

# ADAPTIVE METASURFACE DESIGNS FOR THERMAL CAMOUFLAGE, RADIATIVE COOLING, AND PHOTODETECTOR APPLICATIONS

A THESIS SUBMITTED TO  
THE GRADUATE SCHOOL OF ENGINEERING AND SCIENCE  
OF BILKENT UNIVERSITY  
IN PARTIAL FULFILLMENT OF THE REQUIREMENTS FOR  
THE DEGREE OF  
MASTER OF SCIENCE  
IN  
ELECTRICAL AND ELECTRONICS ENGINEERING

By  
Ebru BUHARA  
January 2022

ADAPTIVE METASURFACE DESIGNS FOR THERMAL CAM-  
OUFLAGE, RADIATIVE COOLING, AND PHOTODETECTOR  
APPLICATIONS

By Ebru BUHARA

January 2022

We certify that we have read this thesis and that in our opinion it is fully adequate,  
in scope and in quality, as a thesis for the degree of Master of Science.

---

Ekmel Özbay (Advisor)

---

Vakur Behçet Ertürk

---

Sefer Bora Lisesivdin

Approved for the Graduate School of Engineering and Science:

✓ Ezhan Karışan  
Director of the Graduate School

# ABSTRACT

## ADAPTIVE METASURFACE DESIGNS FOR THERMAL CAMOUFLAGE, RADIATIVE COOLING, AND PHOTODETECTOR APPLICATIONS

Ebru BUHARA

M.S. in Electrical and Electronics Engineering

Advisor: Ekmel Özbay

January 2022

Metamaterials, described as artificial sub-wavelength nanostructures, refer to a class of manufactured materials that possess distinctive electromagnetic features which cannot be found with natural materials. Thermal tunability, negative refractive index, perfect absorption, and invisible cloaking are examples of these attributes. Here, we design and implement metamaterials in four important application areas, namely 1) Multi-spectral infrared camouflage through excitation of plasmon-phonon polaritons in a visible-transparent hBN-ITO nanoantenna emitter, 2) Adaptive visible and short-wave infrared camouflage using a dynamically tunable metasurface, 3) Mid-infrared adaptive thermal camouflage using a phase-change material coupled dielectric nanoantenna, 4) An All-Dielectric Metasurface Coupled with Two-Dimensional Semiconductors for Thermally Tunable Ultra-narrowband Light Absorption.

In the first work, a metasurface design is developed to provide adaptive camouflage in both visible and SWIR ranges. The proposed metasurface is made of an indium tin oxide (ITO) grating on a metal-insulator-metal (MIM, Ag-Sb<sub>2</sub>S<sub>3</sub>-Ag) nanocavity. In the amorphous state, the design operates as a colored transmissive window while, in the crystalline phase, it switches into a reflective mirror. In the meantime, the cavity acts as a thermally tunable host for the ITO nanoantenna providing tunable SWIR absorption to cover two transmissive regions at 1150-1350 nm (Region I) and 1400-1700 nm (Region II). It is found that the excitation of extended surface plasmons (ESPs) and guided mode resonances (GMRs) are responsible for light absorption in the SWIR range. Our theoretical calculations show that, besides the design's ability for color adoption, the SWIR reflectance in Region I/Region II are reduced to 0.37/0.53 and 0.75/0.25 in the amorphous/crystalline phases.

In the second work, a hybrid nanoantenna architecture made of ITO-hBN grating is proposed to satisfy all multi-spectral camouflage requirements. In this design, simultaneous excitation of plasmon-phonon polaritons in ITO and hBN leads to broadband absorption in the NTIR range and reflection in MWIR and LWIR ranges. Moreover, the bulk absorption in ITO film provides SWIR mode camouflage. Moreover, to highlight the importance of this hybrid design, the ITO-hBN design is compared with ITO-TiO<sub>2</sub> heterostructure (TiO<sub>2</sub> is a lossless dielectric in our desired ranges). Finally, the camouflage performance of the metasurface is evaluated as the outgoing emission suppression when the metasurface design is on top of the blackbody object.

In the third work, a PCM-dielectric based metasurface nanoantenna emitter design is proposed to achieve low observability at the MIR region by tailoring the spectral emissivity of the design. The proposed thermal nanoantenna emitter is composed of a high index dielectric (silicon (Si) in our case) nanograting on top of a thick silver (Ag) mirror. An ultrathin VO<sub>2</sub> interlayer is embedded within the grating to actively tune its absorption response. The design geometries are adopted to place the resonance wavelengths in the atmospheric absorption windows for thermal camouflage applications. Based on the position of the VO<sub>2</sub> layer, the optical response of the design in the metal phase can be diversely tuned from a narrowband to a broadband thermal emitter. Therefore, upon increase in the surface temperature, the proposed metasurface based thermal nanoantenna emitter turns into a broadband emitter with a stronger radiative thermal emission while it compatibly releases its heat based on the camouflage technology requirement. The proposed design has perfect matching with atmospheric absorption windows so that it can efficiently release its heat without being observed by thermal camera systems. The detectability of the structure by a possible IR sensor is calculated using power calculations over the selected spectra. In addition, due to the hysteresis behavior of VO<sub>2</sub>, the calculations are done separately for cooling and heating conditions.

In the fourth and final work, a dielectric based metasurface platform is proposed to achieve ultra-narrowband light absorption within a monolayer thick TMDC layer. For this purpose, the metasurface design is optimized. Then, this design is coupled with mono and multilayer TMDCs to observe better absorption results. For this purpose, MoS<sub>2</sub>, and WS<sub>2</sub> are chosen as the most commonly

used TMDCs. The coupling of light into Mie resonances, supported by dielectric nanograting, provides narrowband absorption within the TMDC layer. To reach further enhancement, a cavity design is integrated into this dielectric-based metasurface. For the best optimized design, the absorptance efficiency reaches to 0.85 and FWHM stays as narrow as 3.1 nm. Finally, the thermal tunability characteristic of the design is shown, without use of any phase change material. This is achieved due to strong light confinement within the design. Due to this confinement, any small change in the refractive index is seen by the resonant design. Thus, the resonance frequency shifts and thermal tunability is acquired. The thermal sensitivity of the above-mentioned optimized design reaches to 0.0096 nm/°C.

*Keywords:* Metasurface, Metamaterial, Radiative cooler, Photodetector, Thermal camouflage, Visible, Near infrared, Vanadium dioxide, Plasmonic structure, Nanoantenna emitter, Wavelength selectivity.

## ÖZET

# TERMAL KAMUFLAJ, ISINIMLI SOGUTMA VE FOTODEDEKTÖR UYGULAMALARI İÇİN UYARLANABİLİR METASURFACE TASARIMLARI

Ebru BUHARA

Elektrik ve Elektronik Mühendisliği, Yüksek Lisans

Tez Danışmanı: Ekmel Özbay

Ocak 2022

Dalga boyundan küçük yapay nanoyapılar olarak tanımlanan metamalzemeler, doğal malzemelerde bulunamayan ayırt edici elektromanyetik özelliklere sahip üretilmiş bir malzeme sınıfını ifade eder. Termal ayarlanabilirlik, negatif kırılma indisi, mükemmel absorpsiyon ve görünmez perdeleme bu özelliklere örnektir. Burada, metamalzemeleri dört önemli uygulama alanında tasardık ve uyguladık: 1) Görünür-şeffaf bir hBN-ITO nanoanten emitöründe plazmon-fonon polari-tonlarının uyarılması yoluyla çoklu spektral kızılötesi kamuflaj, 2) Uyarlanabilir görünür ve kısa dalga kızılötesi kamuflaj kullanarak dinamik olarak ayarlanabilen bir metayüzey, 3) Faz değiştiren malzeme ile birleştirilmiş dielektrik nanoanten kullanan orta kızılötesi uyarlanabilir termal kamuflaj, 4) Termal olarak ayarlanabilen ultra dar bant ışık emilimi için iki boyutlu yarı iletkenlerle birleştirilmiş tamamen dielektrik meta yüzey.

İlk çalışmada hem görünür hem de SWIR menzillerinde uyarlanabilir kamuflaj sağlamak için bir metasurface tasarımı geliştirildi. Önerilen meta yüzey, bir metal-yalıtkan-metal (MIM, Ag-Sb<sub>2</sub>S<sub>3</sub>-Ag)) nano kovuk üzerinde bir indiyum kalay oksit (ITO) ızgarasından yapılmıştır. Amorf durumda, tasarım renkli bir geçirgen pencere olarak çalışır, kristal fazda ise yansıtıcı bir aynaya dönüşür. Bu sırada kovuk, 1150-1350 nm (Bölge I) ve 1400-1700 nm'de (Bölge II) iki iletim bölgesini kapsayacak şekilde ayarlanabilir SWIR emilimi sağlayan ITO nanoanteni için termal olarak ayarlanabilen bir yuva görevi görür. Genişletilmiş yüzey plazmonlarının (ESP'ler) ve yönlendirilmiş mod rezonanslarının (GMR'ler) uyarılmasının, SWIR aralığında ışık absorpsiyonundan sorumlu olduğu bulunmuştur. Teorik hesaplamalarımız, tasarımın renk benimseme yeteneğinin yanı sıra, Bölge I/Bölge II'deki SWIR yansımalarının amorf/kristal fazlarda 0,37/0,53

ve 0,75/0,25'e düştüğünü göstermektedir.

İkinci çalışmada, tüm çoklu spektral kamuflej gereksinimlerini karşılamak için ITO-hBN ızgarasından yapılmış bir hibrit nanoanten mimarisi önerilmiştir. Bu tasarımda, ITO ve hBN'deki plazmon-fonon polaritonlarının aynı anda uyarılması, NTIR aralığında geniş bant absorpsiyonuna ve MWIR ve LWIR aralıklarında yansımaya yol açar. Ayrıca, ITO filmindeki absorpsiyon, SWIR modu kamufleji sağlar. Ayrıca, bu hibrit tasarımın önemini vurgulamak için, ITO-hBN tasarımı ITO-TiO<sub>2</sub> heteroyapısı (TiO<sub>2</sub> arzu ettiğimiz aralıklarda kayıpsız bir dielektriktir) ile karşılaştırılır. Son olarak, meta yüzeyin kamuflej performansını, meta yüzey tasarımı kara cisim nesnesinin üzerindeki giden emisyon bastırma kabiliyeti ile değerlendirilir.

Üçüncü çalışmada, tasarımın spektral emisyonunu uyarlayarak MIR bölgesinde düşük gözlemlenebilirlik elde etmek için PCM-dielektrik tabanlı bir metasurface nanoanten emitör tasarımı önerilmiştir. Önerilen termal nanoanten yayıcı, kalın bir gümüş (Ag) aynanın üzerinde yüksek indeksli bir dielektrik nano ızgaradan (bizim durumumuzda silikon (Si)) oluşur. Absorpsiyon tepkisini aktif olarak ayarlamak için ızgaraya ultra ince bir VO<sub>2</sub> ara katmanı yerleştirilmiştir. Tasarım geometrileri, termal kamuflej uygulamaları için atmosferik absorpsiyon pencerelerine rezonans dalga boylarını yerleştirmek için ayarlanmıştır. VO<sub>2</sub> katmanının konumuna bağlı olarak, tasarımın metal fazdaki optik tepkisi, dar banttan geniş bant termal yayıcıya çeşitli şekillerde ayarlanabilir. Bu nedenle, yüzey sıcaklığındaki artışla, önerilen meta yüzey tabanlı termal nanoanten emitör, kamuflej teknolojisi gereksinimine dayalı olarak ısıyı uyumlu bir şekilde serbest bırakırken, daha güçlü bir ışımaya termal emisyonuna sahip geniş bantlı bir emitöre dönüşür. Önerilen tasarımın atmosferik soğurma pencereleri ile mükemmel uyumu vardır, böylece termal kamera sistemleri tarafından gözlemlenmeden ısıyı verimli bir şekilde serbest bırakabilir. Yapının olası bir IR sensörü tarafından algılanabilirliği, seçilen spektrumlar üzerinde güç hesaplamaları kullanılarak hesaplanır. Ayrıca VO<sub>2</sub> malzemesinin histerezis davranışından dolayı hesaplamalar soğutma ve ısıtma koşulları için ayrı ayrı yapılmıştır.

Dördüncü ve son çalışmada, tek katmanlı bir TMDC katmanı içinde ultra dar

bant ışık absorpsiyonunu elde etmek için dielektrik tabanlı bir meta yüzey platformu önerilmiştir. Bu amaçla metasurface tasarımı optimize edilmiştir. Daha sonra bu tasarım, daha iyi absorpsiyon sonuçlarını gözlemlemek için tek ve çok katmanlı TMDC'lerle birleştirilir. Bu amaçla, en yaygın kullanılan TMDC'ler olarak MoS<sub>2</sub> ve WS<sub>2</sub> seçilmiştir. Dielektrik nano ızgara tarafından desteklenen ışığın Mie rezonanslarıyla eşleşmesi, TMDC katmanında dar bantlı absorpsiyon sağlar. Daha fazla iyileştirmeye ulaşmak için, bu dielektrik tabanlı metayüzeye bir kovuk tasarımı entegre edilmiştir. En iyi optimize edilmiş tasarımda, soğurma verimliliği 0,85'e ulaşır ve FWHM, 3,1 nm kadar dar kalır. Son olarak, tasarımın termal ayarlanabilirlik özelliği, herhangi bir faz değiştiren malzeme kullanılmadan gösterilmiştir. Bu, tasarımdaki güçlü ışık hapsi nedeniyle elde edilir. Bu ışık hapsi nedeniyle, rezonans tasarımında kırılma indisindeki herhangi bir küçük değişiklik farkedilir. Böylece rezonans frekansı kaymaları ve termal ayarlanabilirlik elde edilir. Yukarıda bahsedilen optimize edilmiş tasarımın termal hassasiyeti 0,0096 nm/°C'ye ulaşır.

*Anahtar sözcükler:* Metayüzey, Metamalzeme, Radyatif soğutucu, Fotodetektör, Termal görünmezlik, Görünür, Yakın kızılötesi, Vanadyum dioksit, Plazmonik yapılar, Nanoanten yayıcı, Dalgaboyu seçiciliği.

## Acknowledgement

Throughout my M.Sc. study, I have received a great deal of support and assistance. First and foremost, I would like to express my genuine appreciation to my advisor Prof. Ekmel Özbay, for the support and opportunities to further my research. I found great inspiration in his ways of thinking in general terms, his positive energy concerning work and personal relationships, his work ethic, and most importantly, his belief in my abilities during my most difficult times. My sincere appreciation goes to Dr. Amir Ghobadi. His genuine interest, willingness to have discussions at any time on our projects contributed immensely to my productive M.Sc's. His feedbacks pushed me to sharpen my thinking and brought my work to a higher level. I have learned many invaluable things from him regarding scientific research and academia. I would also like to thank Prof. Vakur Behcet Erturk and Prof. Sefer Bora Lisesivdin for being on my thesis committee, their open and positive attitudes, and for their valuable comments on my thesis. I thank all the talented engineers of Bilkent University, NANO-TAM/ABMN, and UNAM for their contributions to my projects. I thank my friends and office mates who made my graduate life fun and friendly. From NANOTAM (old building), I would like to thank Bahram Khalichi, Ataollah Kalantari Osgouei, Zahra Rahimian, Veysel Erçağlar, Volkan Ertürk, Tayfur Kaya, Oguz Odabaşı, Ekin Brıcan Boşdurmaz. From Bilkent University, I would like to thank Enes Şeker, Ali Kaan Sünnetçiođlu, Shirin Pirouzkhah, Abdulmalik A. Madigawa, Serdar Şengül for their friendships. Last but not least, I am incredibly grateful to my parents, Esra and H.Mete Buhara, for their limitless love and support for me in every step of my life. You have always been there for me. I am very much thankful to my sisters Emel, Sinem, and my little angel Begüm for their love and unrelenting supports. They are the best sisters anyone can ask for. None of these achievements could have happened without my family. To everyone that deserved mention but failed to find it in the text above, please know that I appreciate and treasure your contributions to this thesis and my life.

# Contents

- 1 Introduction** **18**
- 1.1 Background . . . . . 19
  - 1.1.1 Dynamically tunable metasurface for adaptive visible and short-wave infrared camouflage . . . . . 19
  - 1.1.2 Nanoantenna emitter for multi-spectral infrared camouflage 20
  - 1.1.3 Phase-change material coupled dielectric nanoantenna for mid-infrared adaptive thermal camouflage . . . . . 22
  - 1.1.4 An all-dielectric metasurface for thermally tunable ultra-narrowband light absorption . . . . . 24
- 1.2 Thesis Outline . . . . . 26
  
- 2 Adaptive visible and short-wave infrared camouflage using a dynamically tunable metasurface** **28**
- 2.1 Introduction . . . . . 28
- 2.2 Results and Discussion . . . . . 29

<b>3</b>	<b>Multi-spectral infrared camouflage through excitation of plasmon-phonon polaritons in a visible-transparent hBN-ITO nanoantenna emitter</b>	<b>37</b>
3.1	Introduction . . . . .	37
3.2	Results and Discussion . . . . .	38
<b>4</b>	<b>Mid-infrared adaptive thermal camouflage using a phase-change material coupled dielectric nanoantenna</b>	<b>46</b>
4.1	Introduction . . . . .	46
4.2	Results and Discussion . . . . .	47
<b>5</b>	<b>An all-dielectric metasurface coupled with two-dimensional semiconductors for thermally tunable ultra-narrowband light absorption</b>	<b>61</b>
5.1	Introduction . . . . .	61
5.2	Results and Discussion . . . . .	62
<b>6</b>	<b>Conclusion</b>	<b>70</b>
<b>A</b>	<b>Scientific Contributions</b>	<b>88</b>
A.1	Journal Articles . . . . .	88
A.2	Conference Papers . . . . .	89

# List of Figures

2.1	Transmission spectra of the MIM cavity for different $D_M$ values for the (a) amorphous and (b) crystalline phases. The impact of spacer thickness ( $D_I$ ) on the transmission spectra of the MIM cavity design for the (c) amorphous and (d) crystalline phases. (e) Schematic representation of the optical response of the MIM cavity in the visible range upon phase transition from amorphous to crystalline. (f) Angular response of the MIM cavity. . . . .	30
2.2	(a) Schematic representation of the proposed metasurface with its dimensions P, W, and H. (b) Reflection and transmission data of the metasurface in the amorphous and crystalline phases. The transmission data are bolded in the visible range (350–800 nm), and the reflection data are bolded in the SWIR (900–1800 nm) range. (c) Detection mechanism of the proposed metasurface using a SWIR mode thermal camera. (d) Functionality of the design in the visible and SWIR ranges. The colors shown in this panel are extracted from the Commission Internationale de l’Elclairage (CIE) color map. (e) Angular reflectance response of the metasurface in the amorphous and crystalline phases. The reflection contour plots as a function of the (f) periodicity (P), (g) grating height (H), and (h) grating width (W). In these plots, the other dimensions are kept in their optimal values. . . . .	32

2.3	(a) E-field and (b) absorption profiles across the design in the first resonance mode of $\lambda_1 = 1131$ nm demonstrate the simultaneous excitation of ESPs in the metal-insulator interface and GMRs excited inside the cavity design. (c) E-field and (d) absorption profiles across the design in the first resonance mode of $\lambda_2 = 1275$ nm showing the transmissive FP modes excited in the MIM cavity design. (e) E-field and (f) absorption profiles across the design in the first resonance mode of $\lambda_3 = 1338$ nm indicates the excitation of GMRs inside the cavity. (g) Position of absorption monitors used in our analysis. (h) Absorption profiles within the ITO grating, MIM cavity, and the whole design. . . . .	34
2.4	(a) Reflected solar irradiance from a metal reflector and the metasurface in the amorphous and crystalline phases. (b) Averaged power ratios in three different SWIR ranges. . . . .	36
3.1	(a) Schematic illustration of the nanoantenna design and the absorption contour plots for different (b) w and (c) t. (d) The dependence of the absorption profile to design periodicity. (e) Different detection scenarios of an object. The profiles and their average SWIR, MWIR, and LWIR absorption/reflection/transmission data of the nanoantenna on different substrates of (f)-(g) dielectric and (h)-(i) metal. . . . .	39

3.2	(a) Proposed hBN-ITO nanoantenna design, (b) permittivity data of hBN and TiO <sub>2</sub> , and (c) absorption/reflection spectra of the nanoantenna for both hBN and TiO <sub>2</sub> -based designs. (d) Visible light transmission and reflection of ITO-hBN. The reflection contour plots of the nanoantenna design as a function of grating (e) width, (f) height, and (g) periodicity. The E-field and absorption density profiles across the nanoantenna for different resonance wavelengths of (h) 1.12 μm, (i) 6.15 μm, (j) 6.82 μm, and (k) 7.2 μm. The color bar units for E-field and absorption density are V/m and W/m <sup>2</sup> . . . . .	41
3.3	(a) Schematic illustration of thermal emission pathways from the design on top of a blackbody. (b) Thermal emission comparison of blackbody radiation at room temperature, blackbody radiation under the atmospheric transmission, metasurface design on top of BB, and the real emission from the design. . . . .	45
4.1	(a) Schematic representation and (b) absorption spectra of the proposed nanoantenna emitter. Impact of the nanograting dimensions including (c) the period, (d) width and (e) thickness on the absorption spectra while each parameter of the structure is kept at its optimized value besides the variation of the target parameter. . . . .	48
4.2	(a) Schematic representation of the PCM–dielectric based metamaterial nanoantenna emitter. The contour plots of the absorption amplitude as a function of VO <sub>2</sub> position for (b) insulator and (c) metal phase conditions. The absorption spectra of the structure in both the metallic and insulator phases for two different VO <sub>2</sub> positions at (d) d <sub>1</sub> = 5 nm (design I) and (e) d <sub>1</sub> = 1550 nm (design II). . . . .	50

4.3	Impact of the VO <sub>2</sub> thickness on the absorption spectrum of design I at (a) the insulator phase, (b) the metallic phase, and on the absorption spectrum of design II at (c) the insulator phase, (d) the metallic phase. . . . .	51
4.4	On resonance electric-field distributions across the proposed PCM–dielectric based metamaterial nanoantenna emitter (design II) on the x - y plane for (a)–(d) the cold and (e)–(h) hot states when the position of VO <sub>2</sub> interlayer is d <sub>1</sub> = 1550 nm. The color bar is shown in logarithmic scales for better comparison. The thin VO <sub>2</sub> interlayer is shown as the gray lines within the structure while the Si boundaries are shown as white dashed lines. . . . .	52
4.5	Dispersion diagram of the (a) Ag-Si planar structure and the (b) Ag-Si nanograting structure with the dimensions given in Fig. 4.1(a). . . . .	53
4.6	On resonance absorbed power density distributions across the Ag layer on the x - y plane considering two periodicities for (a), (b) the cold and (c), (d) hot states when the position of VO <sub>2</sub> interlayer is d <sub>1</sub> = 1550 nm. On resonance absorbed power density distributions across the VO <sub>2</sub> layer on the x - y plane considering two periodicities for (e), (f) the cold and (g), (h) hot states when the position of VO <sub>2</sub> interlayer is d <sub>1</sub> = 1550 nm. . . . .	57
4.7	. (a) Schematic illustration of the detected optical power density using IR thermal cameras emitted from the proposed PCM–dielectric based metamaterial nanoantenna emitter. Emitted power density calculations of design I given in a logarithmic scale for different intervals including (b) 3 - 4 μm, (c) 4 - 4.2 μm, (d) 4.2 - 5 μm, (e) 5 - 8 μm, and (f) 8 - 12 μm. . . . .	58
4.8	Emitted power density calculations of design II given in a logarithmic scale for different intervals including (a) 3 - 4 μm, (b) 4 - 4.2 μm, (c) 4.2 - 5 μm, (d) 5 - 8 μm, and (e) 8 - 12 μm. . . . .	59

4.9	Comparisons among the emitted power densities at different temperatures including blackbody radiation (black solid line), atmospheric transmissivity for 5 km long transmission path through the atmosphere at the ground level (green dashed-dotted line) over the corresponding blackbody radiation, the proposed structure without considering atmospheric transmissivity (blue solid line) over the corresponding blackbody radiation, and the real emission response of the proposed design I and II (red solid line). The emitted power densities of the proposed narrowband design at the (a) cold state when the temperature is 25 °C and (b) hot state when the temperature is 90 °C. The emitted power densities of the proposed broadband design at the (c) cold state when the temperature is 25 °C and (d) hot state when the temperature is 90 °C. . . . .	60
5.1	(a) Schematic representation of the proposed dielectric metasurface structure. H-field and E-field distributions across the design for (b, c) resonance frequency and (d, e) off-resonance region. Contour plots of magnetic field intensity dependence to (f) thickness and (g) width . . . . .	63
5.2	(a) Schematic representation of the all-dielectric narrow-band absorber structure, absorption calculation for varying thickness and width of TiO <sub>2</sub> with MoS <sub>2</sub> (b–c) and WS <sub>2</sub> (d–e). (f) The band alignment between Au and MoS <sub>2</sub> layer before and after applying bias. The simulated photocurrent values generated by TMD monolayers in (g) MoS <sub>2</sub> and (h) WS <sub>2</sub> cases. . . . .	64
5.3	Absorption calculation for varying (a) thickness and (b) width of TiO <sub>2</sub> with 5 Layer WS <sub>2</sub> and varying (c) thickness and (d) width of TiO <sub>2</sub> with 10 Layer WS <sub>2</sub> . . . . .	66
5.4	(a) Proposed optimized cavity design and (b) its absorption profile across the cavity with MoS <sub>2</sub> and absorption calculation for varying thickness and width of TiO <sub>2</sub> with MoS <sub>2</sub> (c–d) and (e–f) WS <sub>2</sub> . . .	67

5.5 (a) Schematic illustration of red-shift of the absorption peak as the temperature is increased. Absorption calculation for varying refractive index of TiO<sub>2</sub> with (b) MoS<sub>2</sub> and (c) WS<sub>2</sub> in the proposed design and thermal sensitivity plots with different temperature for (d) MoS<sub>2</sub> and (e) WS<sub>2</sub> . . . . . 69

# Chapter 1

## Introduction

This chapter is one part reprinted with permission from: **Ebru Buhara**, Amir Ghobadi, Ekmel Ozbay, Adaptive visible and short-wave infrared camouflage using a dynamically tunable metasurface, *Optics Letters*, 2021, Vol. 46, Issue 19, pp. 4777-4780, DOI: 10.1364/OL.439435, **Ebru Buhara**, Amir Ghobadi, Ekmel Ozbay, Multi-spectral infrared camouflage through excitation of plasmon-phonon polaritons in a visible-transparent hBN-ITO nanoantenna emitter ,2021, *Optics Letters*, Vol. 46, Issue 19, pp. 4996-4999. DOI: 10.1364/OL.437933, **Ebru Buhara**, Amir Ghobadi, Bahram Khalichi, Hasan Kocer, Ekmel Ozbay, Mid-infrared adaptive thermal camouflage using a phase- change material coupled dielectric nanoantenna, 2021, *Journal of Physics D: Applied Physics*, 54 265105. DOI: 10.1088/1361-6463/abf53d, **Ebru Buhara**, Amir Ghobadi, Ekmel Ozbay, An All-Dielectric Metasurface Coupled with Two-Dimensional Semiconductors for Thermally Tunable Ultra-narrowband Light Absorption, 2020, *Plasmonics*, 16, 687–694. DOI: 10.1007/s11468-020-01330-4

## 1.1 Background

”Meta” is a word with a Greek origin that means beyond. ”Metamaterials,” which derives from it, are three-dimensional materials that show exotic properties beyond natural materials [1]. Their two-dimensional counterparts are called metasurfaces [2]. These materials demonstrate unique properties such as negative refraction [3, 4], artificial magnetism [5], asymmetric transmission [6], cloaking [7, 8], and lasing [9, 10] due to the structure of the materials they are formed of. The first work done about metamaterials belonged to V.G. Veselago who said materials with negative permittivity and permeability is theoretically possible in 1968 [11]. After the first work, many researchers have worked on metamaterials to extract their potential in various fields [12, 13, 14, 15]. Metamaterials display strong light-matter interactions which can lead to harvesting electromagnetic radiation in a narrowband or broadband response. According to this response, the metamaterial can be used in sensing [16, 17], imaging [18, 19], and colorfiltering [20, 21] or thermal photovoltaics [22], hot-electron based photodetectors [23] and radiative cooling [24].

This thesis investigates four essential applications areas of metasurfaces, 1. Dynamically tunable metasurface for adaptive visible and short-wave infrared camouflage, 2. Nanoantenna emitter for multi-spectral infrared camouflage, and 3. Phase-change material coupled dielectric nanoantenna for mid-infrared adaptive thermal camouflage, 4. An all-dielectric metasurface for thermally tunable ultra-narrowband light absorption.

### 1.1.1 Dynamically tunable metasurface for adaptive visible and short-wave infrared camouflage

Active metasurfaces with a dynamically tunable optical response have been a long-standing goal because they promise extendable and reconfigurable functionalities [25]. Among the different applications, tunable color filters are some of

the most promising applications of active metasurfaces [26]. A commonly used approach to fabricate actively tunable color filters is to use phase change materials (PCMs), such as vanadium dioxide [27, 28], germanium-antimony-tellurium [29], germanium telluride [30], and antimony trisulfide  $Sb_2S_3$  [31]. Among these,  $Sb_2S_3$  with an amorphous phase in the lower temperatures and a crystalline phase in the higher temperatures ( $>270^\circ$ ) [32], is an ideal material for a thermally tunable color generation, due to its large index contrast between two phases in the visible range.

The equivalence of the color adoption in the longer ranges, such as the infrared region, is thermal camouflage [33]. Therefore, similarly, these PCM-based metasurfaces are used for adaptive thermal camouflage [34, 35, 36]. In general, three thermal camera types are used to detect an object. Short-wave infrared (SWIR, 900–1700 nm), mid-wave infrared (MWIR, 3–5  $\mu\text{m}$ ), and long-wave infrared (LWIR, 8–12  $\mu\text{m}$ ) modes. MWIR and LWIR mode cameras detect the blackbody radiation from a hot matter, while the SWIR mode detects the reflected solar irradiation from an object. The manipulation of the absorption spectrum of a nanoantenna is used as a means to design a proper thermal emitter [37, 38]. The proposed metasurfaces are designed in a way that, in the hot state, the thermal signatures in the MWIR and LWIR ranges are mitigated. This is achieved by the transition from the dielectric to the metal phase with a dominant reflectance response in the above-mentioned ranges or placing emission resonance in the non-transmissive window (5–8  $\mu\text{m}$ ) in the hot state [34, 39]. However, to the best of our knowledge, there is no work on the use of PCMs for SWIR mode camouflage where, unlike the MWIR and LWIR, the solar reflection should be reduced.

### 1.1.2 Nanoantenna emitter for multi-spectral infrared camouflage

Based on the Stefan–Boltzmann law  $P = \varepsilon\sigma T^4$ , the emission from an object is a function of surface emissivity ( $\varepsilon$ ). Based on Kirchoff’s law for thermal radiation

in thermodynamic equilibrium, absorptivity of an object is equal to its emissivity,  $\alpha(T, \lambda) = \varepsilon(T, \lambda)$ . Thus, the manipulation of the absorption spectrum of a nanoantenna can be used as a means to design a proper thermal emitter design [40].

While obtaining thermal camouflage is possible by blocking all the emission wavelengths (for instance, using metallic foils), it causes heat buildup and instability issues. To prevent this, the emitted power should be selectively sent out into the atmosphere in some permitted wavelengths in the non-transmissive atmospheric windows [41, 42]. There are two windows that allow transmission in the infrared region: 3-5  $\mu\text{m}$  [mid-wave infrared (MWIR)] and 8-12  $\mu\text{m}$  [long-wave infrared (LWIR)] ranges. Consequently, the non-transmissive infrared (NTIR) window locates at 5-8  $\mu\text{m}$  wavelengths. Besides this, short-wave infrared (SWIR) (0.9-1.7  $\mu\text{m}$ ) cameras are also used for a target tracking. Unlike MWIR and LWIR mode designs, SWIR cameras detect the surface reflected solar irradiation rather than the blackbody emission. Thus, in an ideal camouflage compatible radiative cooling scenario, the object should be (i) SWIR absorber, (ii) MWIR and LWIR reflector, (iii) NTIR absorber, and (iv) visible transparent to keep its visual appearance and to minimize solar induced heating. The use of metal-based metamaterial/metasurface nanoantennas is a common approach to acquire suppressed emission in MWIR and LWIR regions while allowing radiative cooling in the NTIR window [34, 36, 43, 39]. However, metallic designs do not meet the transparency and SWIR absorbing requirements. Excitation of surface plasmon polaritons (SPPs) in indium tin oxide (ITO) film using a nanounit design is an excellent choice [44, 45]. Moreover, polar materials such as hexagonal boron nitride (hBN) can provide selective mid-infrared (MIR) absorption through excitation of hyperbolic phonon polaritons (HPPs), while maintaining high transparency in visible range (Eg of 6.1 eV, and n of  $\sim 1.85$ ) [46, 47].

### 1.1.3 Phase-change material coupled dielectric nanoantenna for mid-infrared adaptive thermal camouflage

According to Plank’s law, objects emit thermal radiation if the temperature of the structure is above absolute zero [48]. This thermal radiation can be calculated by the Stefan-Boltzmann law that indicates the emission from an object is proportional to the fourth power of the temperature ( $T^4$ ) and the surface emissivity ( $\epsilon$ ) [49]. To find the surface emissivity, Kirchhoff’s law for thermal radiation can be utilized, pointing out that the absorptivity of an object is equal to its emissivity in thermodynamic equilibrium [50]. For an ideal blackbody, which is known as a perfect absorber, the absorptivity therefore the emissivity is unity and, in this case, the radiation will only be dependent on temperature. For other objects, surface emissivity varies from 0 to 1, so the outgoing radiation is a function of both temperature and surface emissivity [51].

Controlling the thermal emission from an object can be accomplished using two different approaches called: (a) temperature control, and (b) surface emissivity control [52]. Compared to the first approach that may require supplementary cooling and heating devices [53], the surface emissivity control is a rather compatible and robust approach to tailoring the thermal emission. Accordingly, the best design to prevent the thermal emission from a hot object in the infrared (IR) region seems to be a highly reflective structure with near-zero emission and near-unity reflection covering the interior hot object. However, the blocking of all the wavelengths can cause a thermal imbalance and lead to heat build-up [54]. Instead of suppressing all of the emission spectrum, the surface heat can be selectively emitted in some spectral regions while it is mitigated in other ranges. These regions are determined according to atmospheric windows in the IR wavelengths. Inside the 3 - 12  $\mu\text{m}$  spectrum, there are non-transmissive windows with near-zero transmission such as 4 - 4.2  $\mu\text{m}$  and 5 - 8  $\mu\text{m}$  [55], where the atmospheric gases including  $\text{N}_2$ ,  $\text{O}_2$ ,  $\text{CO}_2$ , and water vapor can completely absorb the emitted energy, in a relatively short propagation length. In addition, the electromagnetic waves due to thermal radiation can propagate with minimal losses inside the spectrum regions belonging to atmospheric transmissive windows. That is why

thermal camera systems that are used for 24/7 all-weather surveillance operate either in the mid-wave IR spectral band (3 - 5  $\mu\text{m}$ ) or in the long-wave IR range (8 - 12  $\mu\text{m}$ ), while the mid-IR (MIR) camouflage structures are widely designed to operate at the non-transmissive windows to hide from thermal imaging systems and cameras [56, 57, 58, 59]. The atmospheric transmission spectrum ( $T_{atm}$ ) is related to the atmospheric absorption by  $\varepsilon_{atm} = 1 - T_{atm}$ , where they are modeled by considering the US standard atmosphere compositions at the different vertical distances [60].

To reach the desired emission spectrum, metamaterials and metasurfaces made of nano-structured designs are proposed and demonstrated as one of the most effective methods [42, 35, 61, 62, 63] to achieve spectrally selective thermal emitters, and to reduce the surface emittance as well as the emitted power from the surfaces. This method constitutes one of the main optical paths used in the thermal camouflage technology where the thermal visibility disappears from the selected working wavelength regions [53] or the emissions in the region of interests are selectively suppressed.

Besides utilizing optical metasurface architectures, thermally tunable active phase change materials (PCMs), such as germanium antimony telluride (GeSbTe or GST) chalcogenide [64, 65, 66], perovskite manganese oxide [67], samarium nickel oxide ( $\text{SmNiO}_3$ ) [68], and most importantly vanadium dioxide ( $\text{VO}_2$ ) [69], can be used as an ideal scheme to control the thermally tuned optical response. The usage of PCMs with diverse optical properties brings up a unique solution in different technologies [70]. In particular, due to the temperature-dependent optical features of the PCM, these materials are promising candidates for emissivity engineering applications [71, 72, 73]. However, the insulator-to-metal transition (IMT) temperatures of the PCMs are the forcing factor that can affect the desired results. For instance, the IMT temperatures of GST and perovskite manganese oxide [66, 65] are around 150  $^\circ\text{C}$  and 10  $^\circ\text{C}$ , respectively, and  $\text{SmNiO}_3$  becomes gradually more metallic from room temperature to 140  $^\circ\text{C}$  [68]. Therefore, in our design procedure,  $\text{VO}_2$  with an IMT temperature around 68  $^\circ\text{C}$  and rapid change around this temperature can be an appropriate choice for the thermal camouflage applications from room temperature to 90  $^\circ\text{C}$  [36, 74, 75, 76]. Not only that, this

matchless switching feature of VO<sub>2</sub> results in various applications, such as IR sensors [77], memristors electronic memories [78], telecommunication modulators [79], and smart windows [80]. The crystal structure of VO<sub>2</sub> in the insulator phase (in the lower temperatures) is a monoclinic, while it turns to tetragonal form and VO<sub>2</sub> dominantly shows metal properties after the temperature of ~68 °C. Although this transition is reversible and provides adaptivity to the temperature variations [81], a VO<sub>2</sub> thin layer can partially absorb the incident light in its metallic phase without showing any wavelength selective properties, while the amount of absorption is negligible in the insulator phase. Metamaterials, on the other hand, are selective absorbers with adjustable (narrow/broad) spectral responses [82], but they are passive structures with no temperature sensitivity. Therefore, a hybrid design made of metamaterial absorbers and VO<sub>2</sub> thin films can provide an opportunity to realize spectrally selective active thermal nanoantenna emitters.

#### **1.1.4 An all-dielectric metasurface for thermally tunable ultra-narrowband light absorption**

In recent years, two-dimensional (2D) materials such as graphene, hexagonal boron nitride, and transition metal dichalcogenides (TMDCs) have been attractive research topics due to their exotic electrical, optical, and mechanical properties and their suitability for usage in the future 2D electronic and optoelectronics [83, 84, 85, 86]. This interest started after the first extraction from graphite using the mechanical exfoliation method of graphene, and since then, graphene has become one of the most intensively studied topics in the field of 2D materials [87, 88, 89, 90]. Although it attracts tremendous attention and it is used in electronic device development, graphene is an inconvenient substance for digital and optoelectronic applications due to the lack of optical bandgap [91]. This absence caused the focus of the 2D material research to shift to the TMDCs [92, 93, 94, 95].

TMDCs are semiconductors in the form of MX<sub>2</sub>, in which M is a transition metal atom and X is a chalcogen element. The metal atom in the middle bond

covalently to the chalcogen atoms and this bonding constructs a sandwich form in the single layer [96]. Although they have a strong covalent bond in-plane, their out-of-plane bonding is weak due to the van der Waals interactions. Because of that they are able to stay stable, even in the monolayer form [97]. Also, with the help of this weak bonding in out-of-plane, they can be obtained as a monolayer by mechanical exfoliation called as the “Scotch-tape” method [98]. In addition, the synthesis of thin-film TMDCs has been achieved at wafer-scale by metal-organic chemical vapor deposition (MOCVD) [99], and small-scale with chemical vapor deposition (CVD) [100].

As a special TMDC semiconductor, monolayer molybdenum disulfide ( $\text{MoS}_2$ ) arouse the interest of many researchers [101, 102, 103]. Similar to other TMDCs, the  $\text{MoS}_2$  experiences an indirect to direct bandgap transition (from 1.3 to 1.8 eV) when it turns to monolayer from bulk [104]. Thus, this transition significantly improves photoluminescence and absorption dynamics of the material. Moreover, monolayer  $\text{MoS}_2$  with a thickness of 0.65 nm has a flexible mechanics due to its high Young’s modulus [105], and it has also high carrier mobility and high on-off ratio up to 109 [106]. These properties promise flexible, high-performance, small, and light optoelectronic devices such as ultra-fast detector, field-effect transistors, and photovoltaic cells [107]. Especially high absorption coefficient and bandgap in the visible range makes  $\text{MoS}_2$  ideal for 2D optoelectronic device applications [101].  $\text{MoS}_2$  gives about 39- and 13-times higher absorption if it is compared with traditional materials such as Si and GaAs in 1-nm layer thickness. Despite its superiority over traditional materials in atomic scale dimension, monolayer  $\text{MoS}_2$  itself absorbs only  $\sim 10\%$  of incident light [108]. Weak absorption due to their extremely thin thickness is the major problem in the way of their use in photoconversion systems. Thus, this 2D semiconductor should be coupled with a trapping scheme to increase its light absorption [109].

To be able to enhance this absorption feature of the TMDCs towards the unity, three main trapping schemes can be employed: (i) metal-based plasmonic [110, 111, 112, 113, 114, 115], (ii) guided mode resonance [116, 117, 118, 119], and (iii) photonic crystal [120, 121, 122]-based designs. Although plasmonic structures

are common solution to enhance the light-matter interaction in TMDC-based absorbers, metals cause parasitic absorption (Joul loss) due to their larger extinction coefficient (compared with that of TMDCs). Thus, the most of the light is consumed in metal parts and absorption efficiency within the TMDC monolayer is low. Moreover, they have large full-width-at-half-maximum (FWHM), due to the fact that the surface plasmon resonances (SPRs) have relatively broad spectral coverage [123]. Guided mode resonance-based designs can provide higher absorption efficiencies (due to their low-loss material nature); however, they have also large FWHM values. Photonic crystal-integrated designs have also bulky nature with multiple fabrication routes, which violates the 2D advantage of these TMDC based designs. Thus, in an ideal scheme, we need to have a lossless and 2D trapping architecture to maximize light coupling into TMDC monolayer. This can be achieved with all-dielectric-based metasurface designs that support the excitation of Mie resonances. Dielectric-based designs are lowloss alternatives of metallic designs and have found many applications, in recent years [124, 125, 126, 82, 127]. With the help of Mie resonance, the plasmonic effect can be replicated and the lossless characteristic of the dielectrics can provide a narrow spectral range light confinement, with high absorption efficiency. In addition to these features, the strong light confinement in the dielectric medium can provide high sensitivity into refractive index change. This will provide the opportunity to manipulate the absorption peak response. In other words, this structure can provide thermal tunability without the use of any phase-change material.

## 1.2 Thesis Outline

In chapter 2, a metasurface design is developed to provide adaptive camouflage in both visible and SWIR ranges. The proposed metasurface is made of an indium tin oxide (ITO) grating on a metal-insulator-metal (MIM, Ag -  $\text{Sb}_2\text{S}_3$  - Ag) nanocavity. In the amorphous state, the design operates as a colored transmissive window while, in the crystalline phase, it switches into a reflective mirror.

In chapter 3, a hybrid nanoantenna architecture made of ITO-hBN grating is proposed to satisfy all multi-spectral camouflage requirements. In this design, simultaneous excitation of plasmon-phonon polaritons in ITO and hBN leads to broadband absorption in the NTIR range and reflection in MWIR and LWIR ranges.

In chapter 4, PCM–dielectric based metasurface nanoantenna emitter design is proposed to achieve low observability at the MIR region by tailoring the spectral emissivity of the design. The proposed thermal nanoantenna emitter is composed of a high index dielectric (silicon (Si) in our case) nanograting on top of a thick silver (Ag) mirror. An ultrathin VO<sub>2</sub> interlayer is embedded within the grating to actively tune its absorption response. The design geometries are adopted to place the resonance wavelengths in the atmospheric absorption windows for thermal camouflage applications. Based on the position of the VO<sub>2</sub> layer, the optical response of the design in the metal phase can be diversely tuned from a narrowband to a broadband thermal emitter.

In chapter 5, we propose a dielectric based metasurface platform to achieve ultra-narrowband light absorption within a monolayer thick TMDC layer. For this purpose, we first optimize the metasurface design itself. Then, we couple this design with mono and multilayer TMDCs to observe better absorption results. For this purpose, we choose MoS<sub>2</sub>, and WS<sub>2</sub> as the most commonly used TMDCs. The coupling of light into Mie resonances, supported by dielectric nanograting, provides narrowband absorption within the TMDC layer. To reach further enhancement, a cavity design is integrated into this dielectric-based metasurface. For the best optimized design, the absorptance efficiency reaches to 0.85 and FWHM stays as narrow as 3.1 nm.

Finally, chapter 6 presents a conclusion on the thesis.

## Chapter 2

# Adaptive visible and short-wave infrared camouflage using a dynamically tunable metasurface

This chapter is one part reprinted with permission from: **Ebru Buhara**, Amir Ghobadi, Ekmel Ozbay, Adaptive visible and short-wave infrared camouflage using a dynamically tunable metasurface, *Optics Letters*, 2021, Vol. 46, Issue 19, pp. 4777-4780, DOI: 10.1364/OL.439435

### 2.1 Introduction

In this section, a metasurface design is developed to provide adaptive camouflage in both visible and SWIR ranges. The proposed metasurface is made of an indium tin oxide (ITO) grating on a metal-insulator-metal (MIM, Ag -  $Sb_2S_3$  - Ag) nanocavity. In the amorphous state, the design operates as a colored transmissive window while, in the crystalline phase, it switches into a reflective mirror. In the meantime, the cavity acts as a thermally tunable host for the ITO

nanoantenna providing tunable SWIR absorption to cover two transmissive regions at 1150–1350 nm (Region I) and 1400–1700 nm (Region II). It is found that the excitation of extended surface plasmons (ESPs) and guided mode resonances (GMRs) are responsible for light absorption in the SWIR range. Our theoretical calculations show that, besides the design’s ability for color adoption, the SWIR reflectance in Region I/Region II are reduced to 0.37/0.53 and 0.75/0.25 in the amorphous/crystalline phases.

## 2.2 Results and Discussion

To begin with, first the MIM cavity is optimized to achieve a mirror/window transition upon phase transition. The top and bottom metals are Ag (Johnson and Christy model [128]) with an identical thickness of  $D_M$ . The insulator is  $Sb_2S_3$  with a thickness of  $D_I$  and the permittivity data obtained from a previous study [32]. Simulations are performed using the Lumerical Finite-Difference Time-Domain software [129] For this aim, we first fix the  $D_I$  in 40 nm, and sweep the  $D_M$  to find the best metal thickness. As shown in Figs. 2.1(a) and 2.1(b), as the metal becomes thicker, the full-width at half-maximum (FWHM) of the transmission resonance gets narrower. However, for layers thicker than 15 nm, the transmission amplitude also reduces. Therefore, in a  $D_M = 15$  nm, we have a right trade-off between the amplitude and FWHM of the transmissive color filter. Next, we fixed the metal layer thickness in its optimal value of 15 nm and tune the spacer thickness to find the proper dimension to have mirror–window transition, as shown in Figs. 2.1(c) and 2.1(d). For this, the  $D_I$  thickness is swept from 20 to 60 nm. The resonance wavelength of the amorphous phase MIM cavity is located at 670 nm, while the design is dominantly reflective in the crystalline mode. Therefore, in these optimized geometries, the MIM cavity acts as a mirror in the hot phase and a colored window in the cold state. This has been schematically shown in Fig. 2.1(e). Moreover, the proposed design retains its color over wide incident angles as depicted in Fig. 2.1(f).

In the next step, this functionality should be extended toward the SWIR range

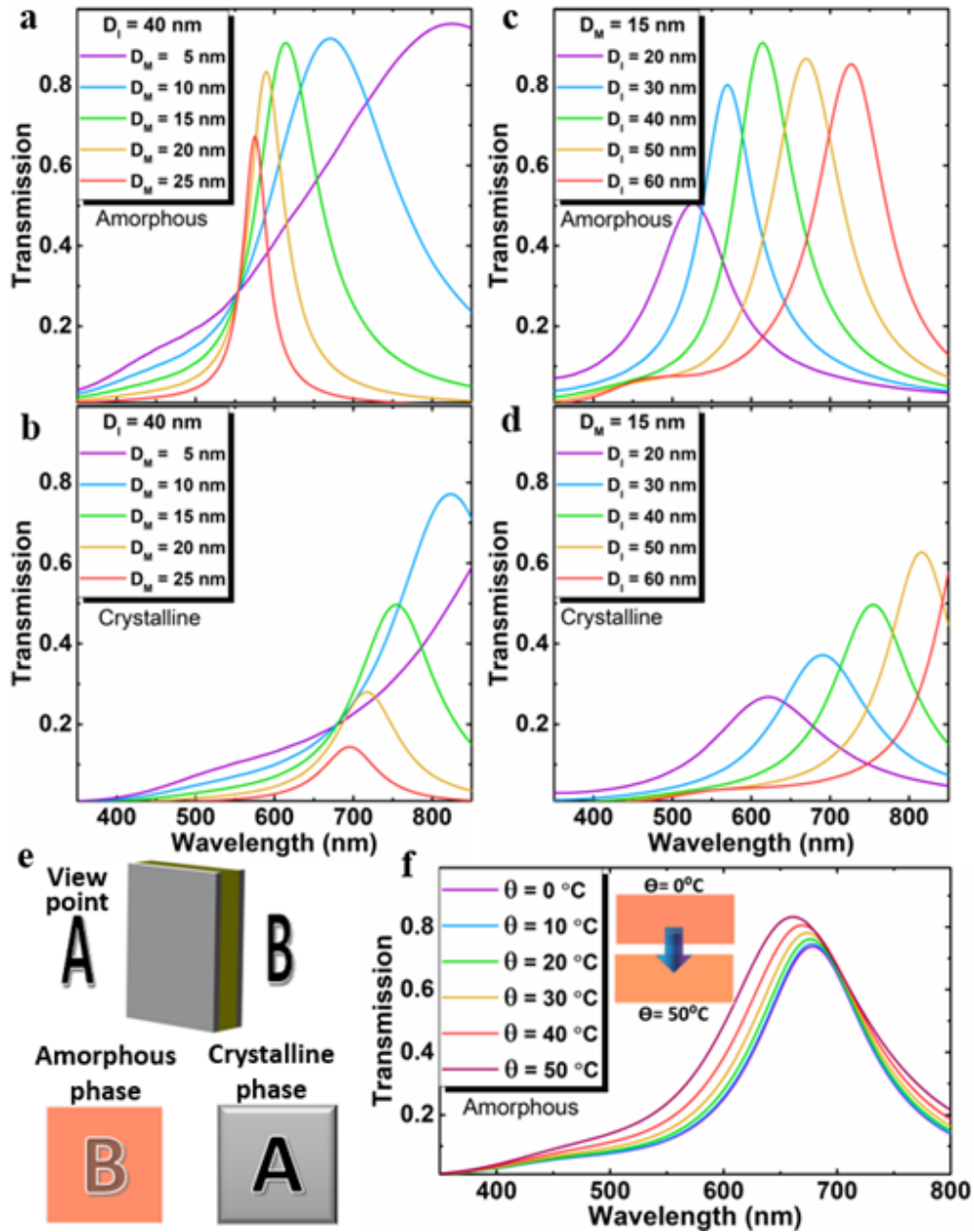


Figure 2.1: Transmission spectra of the MIM cavity for different  $D_M$  values for the (a) amorphous and (b) crystalline phases. The impact of spacer thickness ( $D_I$ ) on the transmission spectra of the MIM cavity design for the (c) amorphous and (d) crystalline phases. (e) Schematic representation of the optical response of the MIM cavity in the visible range upon phase transition from amorphous to crystalline. (f) Angular response of the MIM cavity.

to provide anti-reflection in the 900–1700 nm range. For this, the MIM cavity is coupled into a grating design to excite the resonant modes in the SWIR. In the meantime, the grating material should not disturb the visible response of the MIM cavity. This requirement can be satisfied with the ITO material. Besides building a resonant absorptive metasurface in the SWIR range, to further suppress the reflection in this range, higher-order Fabry–Perot (FP) modes can also be excited. Therefore, the cavity is redesigned to have resonant transmission in both visible and SWIR ranges. For this aim, the spacer layer thickness is increased to 155 nm. The schematic representation of the design is presented in Fig. 2.2(a). The ITO grating layer has a width of  $W$ , height of  $H$ , and periodicity of  $P$ . These three dimensions are optimized to achieve resonant absorption’s at Region I (for amorphous phase) and Region II (for crystalline phase). The optimized design has a periodicity of 1060 nm, grating width of 420 nm, and height of 250 nm. The spectral reflection (R) and transmission (T) data of the metasurface in both phases are depicted in Fig. 2.2(b). In the amorphous phase, the SWIR response consists of three resonant dips located at  $\lambda_1 = 1131$  nm,  $\lambda_2 = 1275$  nm, and  $\lambda_3 = 1338$  nm. Upon the phase change, the resonances are red-shifted to  $\lambda_1 = 1156$  nm,  $\lambda_2 = 1550$  nm, and  $\lambda_3 = 1579$  nm. In the meantime, the visible light transmission response is quite similar to the MIM cavity design, which is expected considering the transparency of ITO and its small filling fraction. Considering the scenario shown in Fig. 2.2(c), the proposed metasurface can simultaneously satisfy the visible and SWIR mode camouflage requirements. In the hot state, the metasurface is a purple-like mirror with anti-reflection capability in Region II of the SWIR range. In the cold state, the design turns into an orange transmissive color filter, and the SWIR response is moved to Region I, as shown in Fig. 2.2(d). The angular response of the design has also been studied to examine the tolerance of the resonance modes against incidence angle change. As Fig. 2.2(e) implies, the visible response that defines the color of the metasurface is almost intact in oblique irradiation. However, the first and third SWIR resonance modes are greatly affected with the angle of incidence. The first mode blue-shifts, while the third mode experiences a red-shift.

To scrutinize the impact of geometries, the parametric sweeps are performed

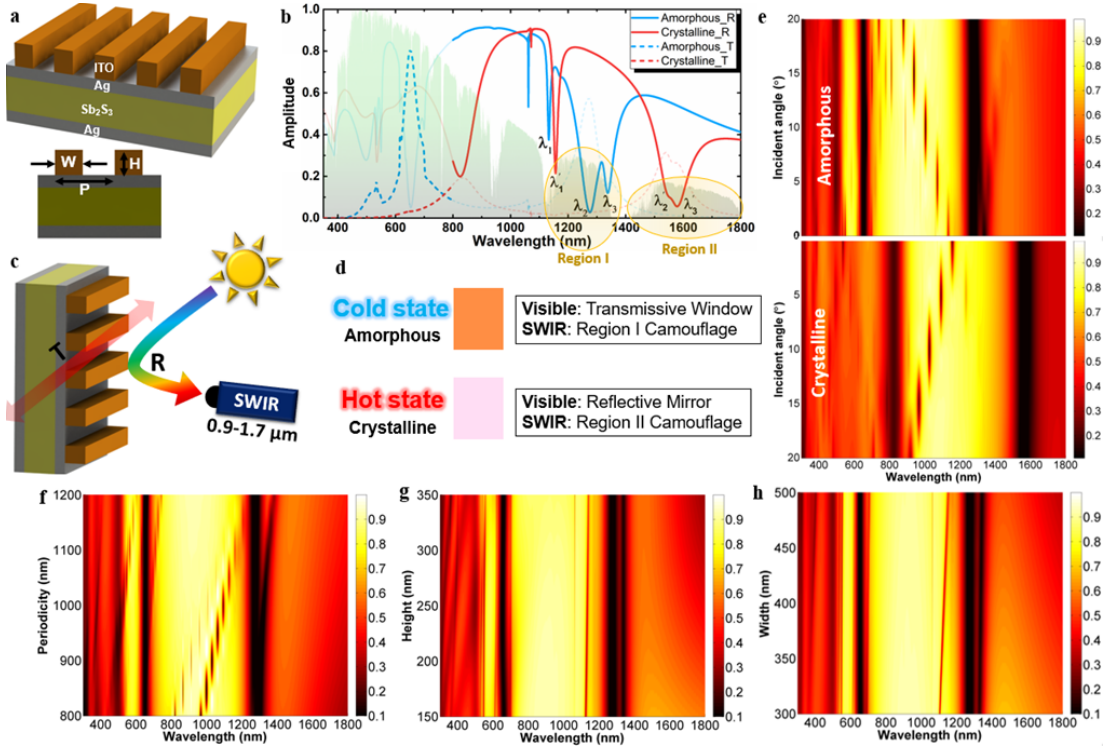


Figure 2.2: (a) Schematic representation of the proposed metasurface with its dimensions  $P$ ,  $W$ , and  $H$ . (b) Reflection and transmission data of the metasurface in the amorphous and crystalline phases. The transmission data are bolded in the visible range (350–800 nm), and the reflection data are bolded in the SWIR (900–1800 nm) range. (c) Detection mechanism of the proposed metasurface using a SWIR mode thermal camera. (d) Functionality of the design in the visible and SWIR ranges. The colors shown in this panel are extracted from the Commission Internationale de l’Eclairage (CIE) color map. (e) Angular reflectance response of the metasurface in the amorphous and crystalline phases. The reflection contour plots as a function of the (f) periodicity ( $P$ ), (g) grating height ( $H$ ), and (h) grating width ( $W$ ). In these plots, the other dimensions are kept in their optimal values.

on the  $W$ ,  $H$ , and  $P$  of the grating, only for the amorphous phase design. Fig. 2.2(f) shows the reflection contour plot as a function of  $P$ . From this panel, the second resonant dip ( $\lambda_2$ ) is insensitive to the periodicity. However, other modes, i.e.,  $\lambda_1$ , and  $\lambda_3$ , slightly shift to longer wavelengths, as the  $P$  widens. Moreover, their resonance strength is also reduced. Therefore, the  $P$  value is fixed at 1060 nm to have all three resonances spectrally adjacent and to provide a broadband anti-reflection to cover the Region I. The other parameter is  $H$ . As plotted in Fig. 2.2(g), the reflection dips spectral position has slight sensitivity to the grating height. However, as the grating thickens, new resonant ripples start to appear in the visible range, and this diminishes the color purity of the design. Moreover, in the longer ranges (1600–1800 nm), a thicker grating causes less reflection, which is a desired response for SWIR mode camouflage. Therefore, the grating height is chosen as 250 nm to have a fair trade-off between color purity and long-range SWIR anti-reflection. Finally, the impact of the  $W$  on different resonance modes is studied. As shown in Fig. 2.2(h), this parameter dominantly affects the first resonance. The wider grating shifts the first mode toward longer wavelengths but, in the meantime, it reduces its resonance strength. Moreover, in the visible range, unwanted resonances start to appear and get boarded as we go toward larger  $W_S$ . To gain an insight into the origin of these resonance modes, the electric field (E-field) and absorption profiles are extracted across the design cross section. Figs. 2.3(a) and 2.3(b) show the E-field and absorption profiles across the design in the  $\lambda_1 = 1131$  nm. Based on [130, 43], this field profile shows the simultaneous excitation of ESPs in the metal-insulator interface and GMRs excited inside the cavity design. The ITO grating acts as a cladding layer to excite the GMRs inside the MIM core. Therefore, the change in grating lateral dimension ( $W$ ) and its periodicity tunes the spectral position of this resonance mode [see Figs. 2.2(f)–2.2(h)]. Looking at the absorption profile of the design, Fig. 2.3(b) shows that the light is harvested in both the ITO grating and MIM cavity design. The excitation of ESPs in the top metal-insulator interface, with long decay lengths extended throughout the ITO layer (as vectorial profile shows), is responsible for light absorption in the ITO layer. Moreover, the excitation of GMRs within the MIM cavity and ESPs in the bottom metal-insulator interface is responsible for light absorption inside the cavity.

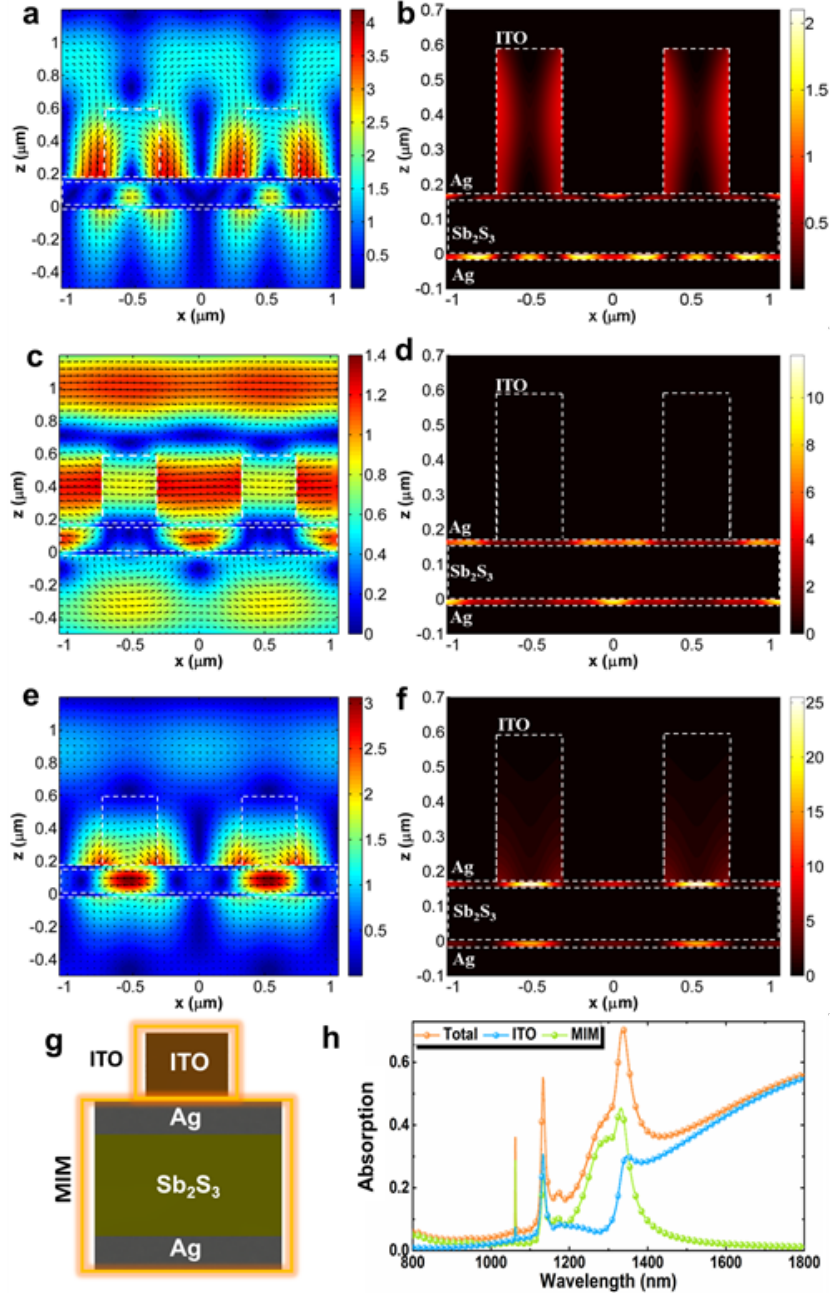


Figure 2.3: (a) E-field and (b) absorption profiles across the design in the first resonance mode of  $\lambda_1 = 1131$  nm demonstrate the simultaneous excitation of ESPs in the metal-insulator interface and GMRs excited inside the cavity design. (c) E-field and (d) absorption profiles across the design in the first resonance mode of  $\lambda_2 = 1275$  nm showing the transmissive FP modes excited in the MIM cavity design. (e) E-field and (f) absorption profiles across the design in the first resonance mode of  $\lambda_3 = 1338$  nm indicates the excitation of GMRs inside the cavity. (g) Position of absorption monitors used in our analysis. (h) Absorption profiles within the ITO grating, MIM cavity, and the whole design.

Similar profiles have also been derived for the second resonance mode located at  $\lambda_2 = 1275$  nm, as shown in Figs. 2.3(c) and 2.3(d). Looking at the wave-front of the incoming light, we can see that the design is transparent in the incoming wave. Therefore, this resonance is the transmissive FP mode that is excited in the MIM cavity design. This can also be seen in the extracted contour plots [Figs. 2.2(f)–2.2(h)], where the second resonance spectral position is independent of the grating dimensions.

Finally, this analysis is performed for the third resonance mode at  $\lambda_3 = 1338$  nm. As shown in Fig. 2.3(e), in this resonance mode, light is dominantly confined inside the MIM cavity design. The E-field profile in this excitation wavelength resembles the excitation of GMRs inside the cavity. Therefore, in this resonance frequency, the active absorption parts are metal layers of the cavity, as shown in Fig. 2.3(f).

The amount of absorbed power inside the MIM cavity and ITO layer is calculated using two monitors, which are shown in Fig. 2.3(g). The absorption spectra within the ITO bulk, the MIM cavity, and the whole design are plotted in Fig. 2.3(h). As we can see in this panel, in the first resonance mode (1131 nm), both components are active, which is due to the simultaneous excitation of ESPs and GMRs. In the second resonance mode, MIM is the active part, which is due to the excitation of FP modes inside the cavity. Finally, in the third mode, MIM has the dominant response, while a part of the absorption belongs to the ITO layer. For longer wavelength ranges, i.e., 1400–1700 nm, the only active part is the ITO layer. This non-resonant absorption is due to the bulk absorption within the ITO layer. Finally, the reflected power from the metasurface in the amorphous and crystalline phase is compared with a metal. For this purpose, the reflection spectra of the design are multiplied with the spectral irradiance of a wavelength solar spectrum, as shown in Fig. 2.4(a). As it can be clearly seen in this figure, the amorphous and crystalline phase metasurface has suppressed reflected power in Region I and Region II, respectively. To have a quantitative comparison, the averaged power ratios (compared to an ideal metal reflector) are extracted for both phases in three wavelength ranges of 900–1700, 1150–1350 (Region I), and 1400–1700 nm (Region II), as shown in Fig. 2.4(b). For this aim, reflected solar

power from the design divided to reflect power from the ideal metal reflector is calculated to understand how much reduction is achieved for each phase in the SWIR range from 900 to 1700 nm. The metasurface has reduced reflected power to 0.66 and 0.7 for the amorphous and crystalline phases, respectively. Moreover, the reduction is examined separately to confirm the anti-reflection capability of phases in different regions. In Region I, this suppression is more pronounced with a ratio of 0.37 for amorphous. For the crystalline phase, the signature reduction is the most effective in Region II with a ratio of 0.25.

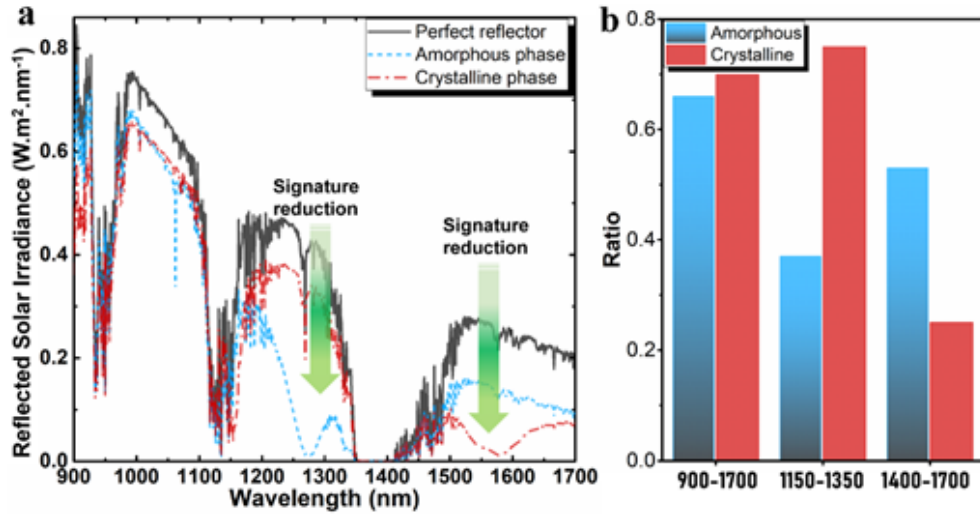


Figure 2.4: (a) Reflected solar irradiance from a metal reflector and the metasurface in the amorphous and crystalline phases. (b) Averaged power ratios in three different SWIR ranges.

## Chapter 3

# Multi-spectral infrared camouflage through excitation of plasmon-phonon polaritons in a visible-transparent hBN-ITO nanoantenna emitter

This chapter is one part reprinted with permission from: **Ebru Buhara**, Amir Ghobadi, Ekmel Ozbay, Multi-spectral infrared camouflage through excitation of plasmon-phonon polaritons in a visible-transparent hBN-ITO nanoantenna emitter ,2021, Optics Letters, Vol. 46, Issue 19, pp. 4996-4999. DOI: 10.1364/OL.437933

### 3.1 Introduction

In this section, a hybrid nanoantenna architecture made of ITO-hBN grating is proposed to satisfy all multi-spectral camouflage requirements. In this design,

simultaneous excitation of plasmon-phonon polaritons in ITO and hBN leads to broadband absorption in the NTIR range and reflection in MWIR and LWIR ranges. Moreover, the bulk absorption in ITO film provides SWIR mode camouflage. Moreover, to highlight the importance of this hybrid design, the ITO-hBN design is compared with ITO-TiO<sub>2</sub> heterostructure (TiO<sub>2</sub> is a lossless dielectric in our desired ranges). Finally, the camouflage performance of the metasurface is evaluated as the outgoing emission suppression when the metasurface design is on top of the blackbody object.

## 3.2 Results and Discussion

Fig. 3.1(a) shows the schematic representation of an ITO-TiO<sub>2</sub> MIR absorber. The ITO is a 1- $\mu\text{m}$ -thick layer, and the TiO<sub>2</sub> is a grating with width of  $w$ , height of  $t$ , and periodicity of  $P$ . To simulate the design, the commercial finite-difference time-domain (FDTD) software package (Lumerical FDTD Solutions) is utilized [129]. These simulations are carried out at two-dimensional (2D) environment, the incident light direction is in the  $y$  direction, the boundary conditions for the  $y$  and  $z$  directions are the periodic and perfectly matched layer (PML), respectively. The permittivity of ITO is extracted from [82] and TiO<sub>2</sub> from [131]. First, the absorption contour plots versus width and the thickness of the grating are extracted, as shown in Figs. 3.1(b) and 3.1(c). In these simulations, the period of the design is chosen as  $P = 4.4 \mu\text{m}$ . The resonance wavelength ( $\lambda_{res}$ ) (at normal incidence) in a metal-dielectric plasmonic design can be expressed as follows [132]:

$$\lambda_{res} = \pm \frac{P}{m} \sqrt{\frac{\epsilon_{metal} \cdot n_{eff}^2}{\epsilon_{metal} + n_{eff}^2}}, \quad (3.1)$$

where  $P$  is periodicity,  $m$  is the diffraction order, and  $n_{eff}$  is the effective refractive index of the SPP mode. In the other side, the  $n_{eff}$  is directly proportional to grating filling factor (or grating width) [133]. This can be seen in Fig. 3.1(b).

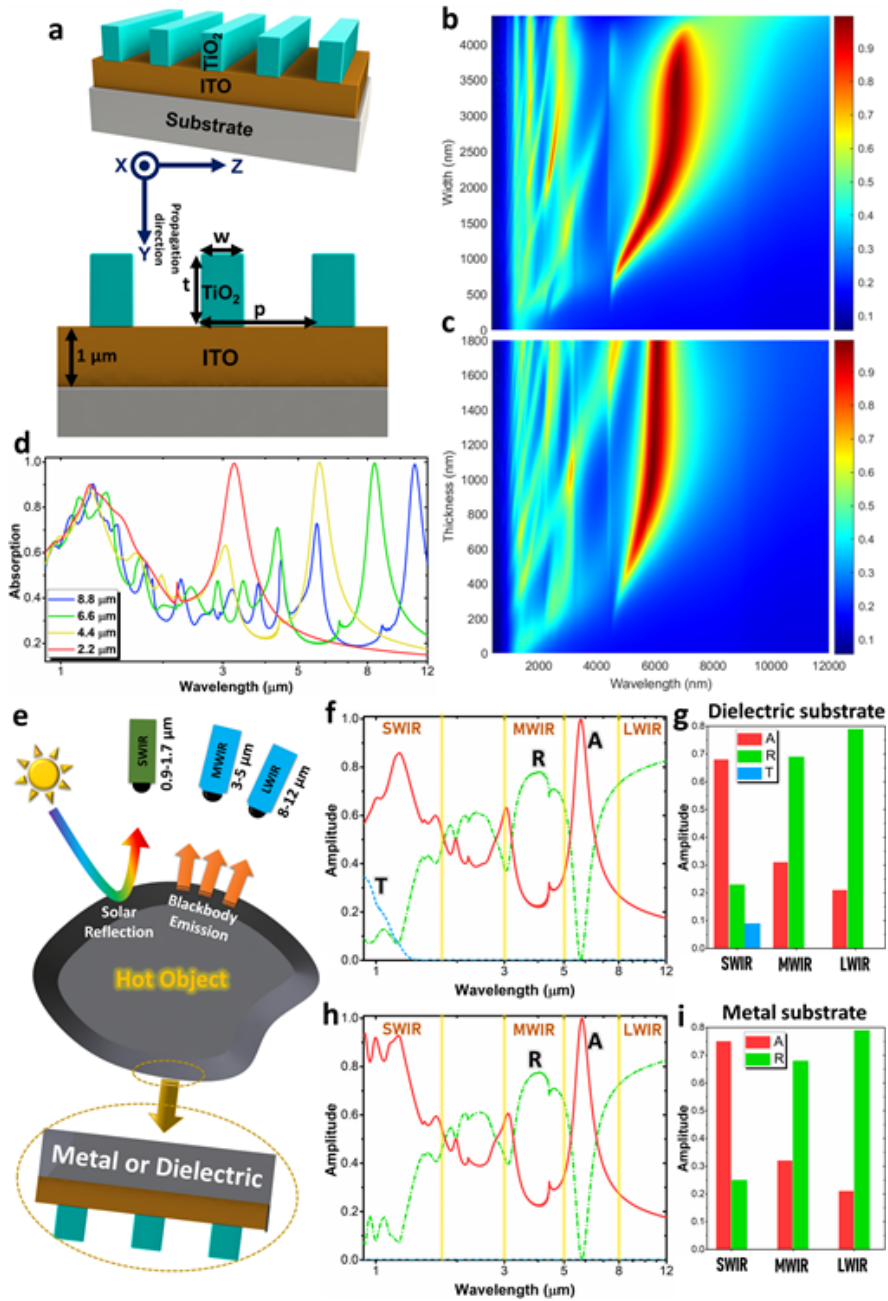


Figure 3.1: (a) Schematic illustration of the nanoantenna design and the absorption contour plots for different (b) *w* and (c) *t*. (d) The dependence of the absorption profile to design periodicity. (e) Different detection scenarios of an object. The profiles and their average SWIR, MWIR, and LWIR absorption/reflection/transmission data of the nanoantenna on different substrates of (f)-(g) dielectric and (h)-(i) metal.

Moreover, it is shown that, upon grating height increase, the  $n_{eff}$  is gradually increased up to some point, and from there it experiences a saturation. This is due to the fact that SPP fields exponentially decay within the grating; after some thickness, they do not see any change in the surrounding environment, and consequently the mode index saturates [134]. This is exactly what we see in Fig. 1(c). Thus, in our case, the alternative plasmonic material, which is ITO, triggers the excitation of SPP modes in the MIR region. To have a strong emission in the NTIR window with minimal signature in MWIR and LWIR ranges, the optimal geometries are chosen as  $w = 1600$  nm and  $t = 900$  nm. Moreover, it should be mentioned that the proposed design is a universal solution to achieve MIR resonant absorption with high optical transparency. To show this, the absorption of the design is simulated for different P values while the  $w/P$  and  $t/P$  ratios are kept same. As we can see from Fig. 1(d), the near perfect absorption resonance in the MIR region is linearly shifted toward longer wavelengths as we increase the periodicity.

The detection mechanisms based on thermal imaging are schematically shown in Fig. 3.1(e). Our above findings prove the functionality of the proposed nanoantenna in spectrally selective engineering of the emitted power. However, it is essential to evaluate its performance on different types of hosts. For this aim, we used two extreme substrate cases of metal and dielectric. The absorption (A), reflection (R), and transmission (T) data for both cases are depicted in Figs. 3.1(f) and 3.1(h). Overall, both designs are dominantly reflective in MWIR and LWIR ranges and have spectral absorption/emission in NTIR range. However, their responses in SWIR range slightly differ. Unlike MIR range, ITO is a low-loss low-index medium in the SWIR regime. Thus, the absorption mechanism is simply the bulk absorption within the ITO film. Therefore, due to the metallic mirror, the optical path length of light within the ITO is enhanced, and consequently larger average absorption values are achieved. The average A, R, and T data have been extracted for both cases in SWIR, MWIR, and LWIR ranges. As seen from Figs. 3.1(g) and 3.1(i), in LWIR and MWIR frequency span, near 80% and 70% of light is reflected, proving its suppressed signature in these ranges. In SWIR, the dielectric platform imposes  $\sim 67\%$  absorption while metallic substrate

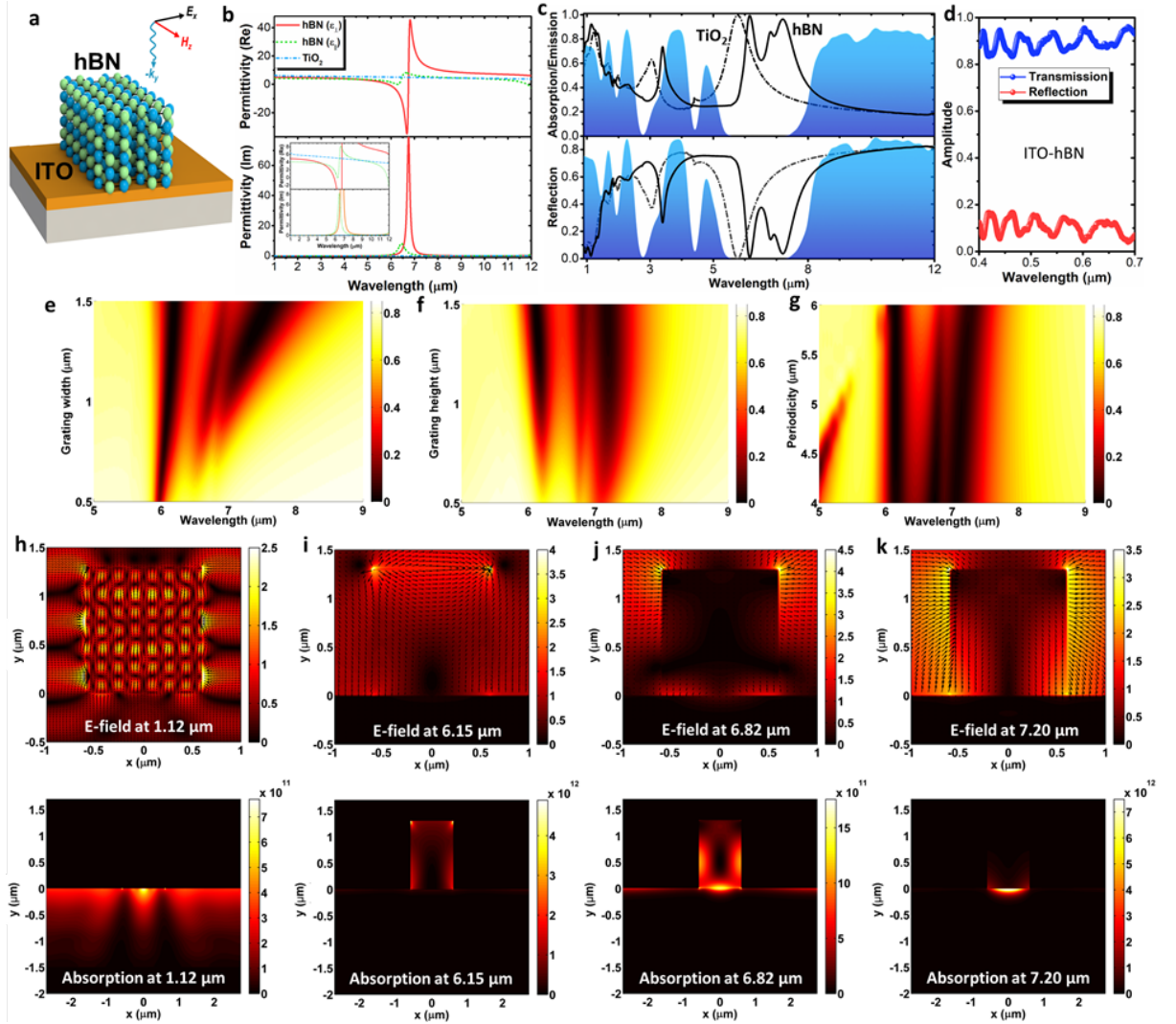


Figure 3.2: (a) Proposed hBN-ITO nanoantenna design, (b) permittivity data of hBN and TiO<sub>2</sub>, and (c) absorption/reflection spectra of the nanoantenna for both hBN and TiO<sub>2</sub>-based designs. (d) Visible light transmission and reflection of ITO-hBN. The reflection contour plots of the nanoantenna design as a function of grating (e) width, (f) height, and (g) periodicity. The E-field and absorption density profiles across the nanoantenna for different resonance wavelengths of (h) 1.12 μm, (i) 6.15 μm, (j) 6.82 μm, and (k) 7.2 μm. The color bar units for E-field and absorption density are V/m and W/m<sup>2</sup>.

absorbs near 76% of the incoming light.

In the next step, we replaced the dielectric grating with a polar material, hBN. Originating from its optical phonon vibrations, hBN naturally possesses MIR Reststrahlen (RS) bands, and one of these bands is located in the NTIR regime. Because of the hyperbolicity in these RS bands, hBN films support multiple orders of low-loss HPP waveguide modes that can potentially be employed to acquire spectrally selective MIR absorption. Thus, the right use of hBN grating on ITO film can provide broader emission (compared to  $\text{TiO}_2$  case) in NTIR region without disturbing its camouflage performance and visible transparency. This architecture can simultaneously excite SPPs in ITO-hBN and HPPs in hBN-air interfaces. The proposed design is exhibited in Fig. 3.2(a). Moreover, the hBN permittivity (both in plane and out of plane parts) is compared with  $\text{TiO}_2$ . As Fig. 3.2(b) implies, the hBN has its RS band in NTIR region, and in the rest of spectrum, it is a lossless dielectric with a permittivity close to  $\text{TiO}_2$ . The R and A responses of optimized  $\text{TiO}_2$ -based and hBN-based thermal nanoantenna emitters have been compared in Fig. 3.2(c). The optimal dimensions of P, w, and t for hBN were found as  $5.5 \mu\text{m}$ ,  $1.2 \mu\text{m}$ , and  $1.3 \mu\text{m}$ . The hBN design has a multiple resonant absorption response in the NTIR region ( $\lambda_1 = 6.15 \mu\text{m}$ ,  $\lambda_2 = 6.82 \mu\text{m}$ ,  $\lambda_3 = 7.2 \mu\text{m}$ ), while it keeps its reflective behavior in the MWIR and LWIR ranges. Moreover, the visible light response of ITO-hBN shows the visual transparency of the design [see Fig. 3.2(d)]. To understand the origin of these resonant modes, parametric sweep on grating width, height, and periodicity is used, as depicted in Figs. 3.2(e)-3.2(g). These contour plots imply that the origin of these resonance modes is different. To gain an insight, the electric field and absorption profiles across the design are extracted for both SWIR and NTIR resonances. As Fig. 3.2(h) plots, the excitation of Fabry-Perot modes is the dominant absorption mechanism, which leads to the bulk absorption within the ITO layer. At the  $\lambda_1$  resonance, a dipolar field profile with two hot spots in the grating edge is observed, and the absorption is dominantly concentrated in the hBN grating [see Fig. 3.2(i)]. The decaying absorption profile (from the air into the hBN bulk), besides hBN optical properties, shows that this mode is a HPP. Due to this nature, the grating width imposes a slight red-shift (corresponding to

the decay length of HPPs in the air-hBN interface) [Fig. 3.2(e)], and periodicity does not affect its spectral position [Fig. 3.2(g)]. The vector field profile of the second mode,  $\lambda_2$ , shows simultaneous excitation of the HPP mode in the hBN wall, and the SPP mode in the hBN-ITO interface. This is also reflected in their absorption profile, where both ITO and hBN are active absorbers [Fig. 3.2(j)]. Thus, this mode is a hybrid SPP-HPP mode, and the gradual red-shift, seen in Fig. 3.2(e), is due to change in  $n_{eff}$  of the grating as explained in Eq. (3.1). Finally, at  $7.2 \mu\text{m}$ , the hBN layer has small  $\text{Im}(\varepsilon)$ , and it acts like a high-index lossless dielectric and excites the SPPs in the ITO layer, as seen in Fig. 3.2(k).

To demonstrate the camouflage character of the design, the metasurface is placed on top of a blackbody radiator (BB) with emissivity of unity [see Fig. 3.3(a)]. The thermal emission from the dotted box is modeled as the sum of three different emissions shown in Eq. (3.2). The first one is the design's own emission calculated using Eq. (3.3). The second one is the transmitted from the design, reflected from the BB and back-transmitted through the metasurface, which is demonstrated in Eq. (3.4). The final one is the emission from the BB transmitted through the design in Eq. (3.5). The blackbody radiation is calculated as in Eq. (3.6). The thermal emission of the design is the multiplication of Eqs. (3.2) and (3.6), which is shown in Eq. (3.7),

$$\varepsilon_{eff}(T, \lambda) = \sum_{j=1}^3 \varepsilon_j(T, \lambda), \quad (3.2)$$

$$\varepsilon_1(T, \lambda) = 1 - R(T, \lambda) - T(T, \lambda), \quad (3.3)$$

$$\varepsilon_2(T, \lambda) = (1 - \varepsilon_{blackbody})T_{back}(T, \lambda)\varepsilon_1(T, \lambda), \quad (3.4)$$

$$\varepsilon_3(T, \lambda) = T_{back}(T, \lambda)\varepsilon_{blackbody}, \quad (3.5)$$

$$BB(T, \lambda) = \frac{2\pi hc^2}{\lambda^5 (e^{\frac{hc}{\lambda kT}} - 1)}, \quad (3.6)$$

$$TE(T, \lambda) = \varepsilon_{eff}(T, \lambda) BB(T, \lambda), \quad (3.7)$$

**Table 3.1 Radiated Amount of Emission.**

Power Density(J/m <sup>2</sup> · s)	BB	TiO <sub>2</sub>	hBN
3–5 μm (at 5 km)	1.321	0.478	0.403
5–8 μm (at surface)	55.956	16.771	29.952
8–12 μm (at 5 km)	61.890	12.298	12.284

Due to the optically thick ITO, no light transmission is occurred; thus,  $T_{back}$  is zero. The radiated power, in a distance of R, is calculated as  $TE(R, T, \lambda) = T_{atm}(R, \lambda) \times TE(T, \lambda)$ , where  $T_{atm}(R, \lambda)$  is the atmospheric transmission at this distance [60]. Using these equations, the spectral emission of BB (300 K) at the surface, BB at 5 km, nanoantenna covered BB at the surface, and nanoantenna covered BB at 5 km have been calculated and compared for both TiO<sub>2</sub> and hBN in Fig. 3.3(b). Radiated powers of the BB, TiO<sub>2</sub>, and hBN are shown in Table 3.1. The TiO<sub>2</sub>-based and hBN-based nanoantenna has reduced BB emission by 71% and 64% in the MWIR range. This reduction is about 81% in the LWIR range. Moreover, the emission at the surface in the NTIR range shows that hBN has not only better camouflage performance but also stronger cooling character [see Fig. 3.3(b)].

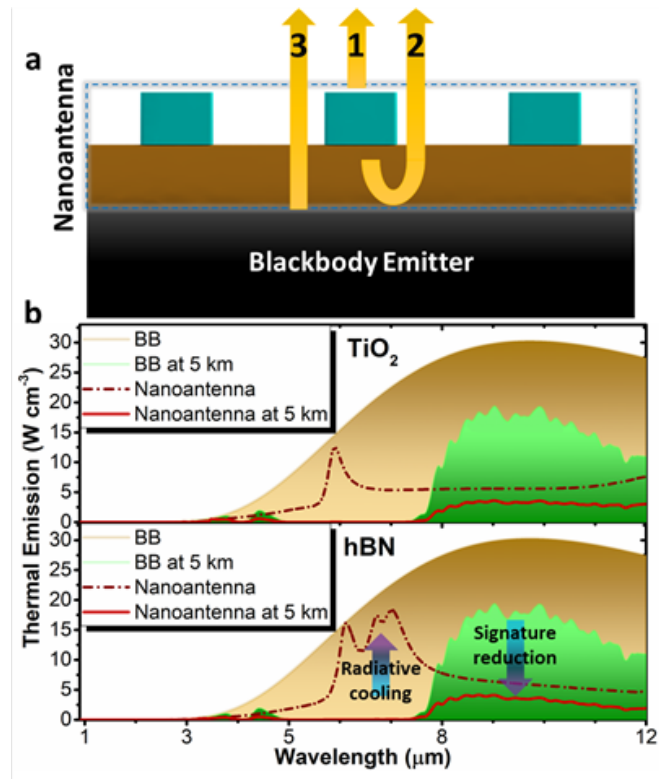


Figure 3.3: (a) Schematic illustration of thermal emission pathways from the design on top of a blackbody. (b) Thermal emission comparison of blackbody radiation at room temperature, blackbody radiation under the atmospheric transmission, metasurface design on top of BB, and the real emission from the design.

# Chapter 4

## Mid-infrared adaptive thermal camouflage using a phase-change material coupled dielectric nanoantenna

This chapter is one part reprinted with permission from: **Ebru Buhara**, Amir Ghobadi, Bahram Khalichi, Hasan Kocer, Ekmel Ozbay, Mid-infrared adaptive thermal camouflage using a phase- change material coupled dielectric nanoantenna, 2021, Journal of Physics D: Applied Physics, 54 265105. DOI: 10.1088/1361-6463/abf53d

### 4.1 Introduction

In this section, a PCM–dielectric based metasurface nanoantenna emitter design is proposed to achieve low observability at the MIR region by tailoring the spectral emissivity of the design. The proposed thermal nanoantenna emitter is composed of a high index dielectric (silicon (Si) in our case) nanograting on top of a thick

silver (Ag) mirror. An ultrathin VO<sub>2</sub> interlayer is embedded within the grating to actively tune its absorption response. The design geometries are adopted to place the resonance wavelengths in the atmospheric absorption windows for thermal camouflage applications. Based on the position of the VO<sub>2</sub> layer, the optical response of the design in the metal phase can be diversely tuned from a narrowband to a broadband thermal emitter. Therefore, upon increase in the surface temperature, the proposed metasurface based thermal nanoantenna emitter turns into a broadband emitter with a stronger radiative thermal emission while it compatibly releases its heat based on the camouflage technology requirement. The proposed design has perfect matching with atmospheric absorption windows so that it can efficiently release its heat without being observed by thermal camera systems. The detectability of the structure by a possible IR sensor is calculated using power calculations over the selected spectra. In addition, due to the hysteresis behavior of VO<sub>2</sub>, the calculations are done separately for cooling and heating conditions.

## 4.2 Results and Discussion

Fig. 4.1(a) is a schematic illustration of the metasurface design, including nanogratings of Si with a constant refractive index of 3.42 on top of Ag resonator (modeling a metallic surface). The spectral refractive index of Ag substrate is taken from the CRC Handbook of Chemistry and Physics [135]. The period, thickness, and width of the Si are set as  $p$ ,  $t$ , and  $w$ , respectively. The commercial finite-difference time-domain (FDTD) software package (Lumerical FDTD Solutions) [129] is employed in calculations to seek out optimum geometries and dimensions. These calculations take place in the 2D simulation region, where the incident light propagation direction is chosen as perpendicular to the  $x - z$  plane (a uniform plane wave propagating along the  $-y$  direction), and the boundary conditions for the  $x$  direction are chosen as an anti-symmetric boundary and perfectly matched layer for the  $y$  direction. A reflection monitor is placed behind the source to integrate the backscattered field, whereas the transmission monitor is located at the front of the source after the structure.

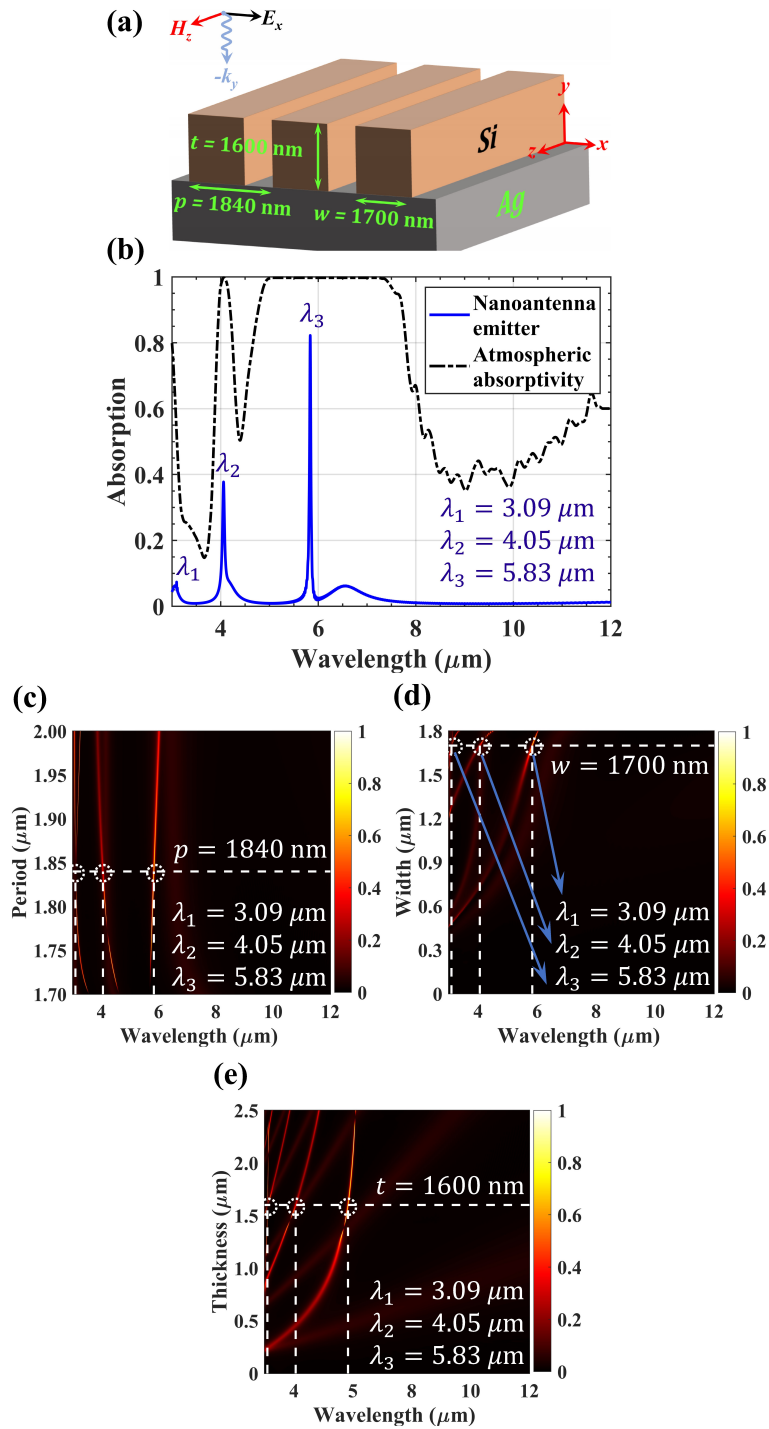


Figure 4.1: (a) Schematic representation and (b) absorption spectra of the proposed nanoantenna emitter. Impact of the nanograting dimensions including (c) the period, (d) width and (e) thickness on the absorption spectra while each parameter of the structure is kept at its optimized value besides the variation of the target parameter.

To be invisible to the IR thermal cameras, the resonance peaks of the nanoantenna emitter should be placed in the high absorption regions (atmospheric absorption windows). The design should reflect back the light in the other wavelengths inside the MIR range. Due to the Ag plate in the bottom of the structure, the transmission through the design is small enough to be ignored. Therefore, the only parameter to be considered in the absorption calculation is the reflection spectrum. In the proposed structure, the resonance wavelengths of the absorption spectrum are dependent on the periodicity, width, and thickness of the nanograting. Accordingly, tuning, extending, or shifting of the resonances mainly rely on rational structural design where the geometrical parameters are optimized in such a way that the occurred resonances in the absorption spectrum match the atmospheric absorption windows as presented in Fig. 4.1(b). Figs. 4.1(c)–(e) represent the absorptivity versus the wavelength for different geometrical parameters while each parameter of the structure is kept at its optimized value besides the variation of the target parameter. It is observed that three resonances can be excited within the atmospheric absorption windows while the dimensions are selected as  $t = 1600$  nm,  $w = 1700$  nm, and  $p = 1840$  nm.

After the optimization of the design, a  $\text{VO}_2$  interlayer is emplaced as shown in Fig. 4.2(a). The  $\text{VO}_2$  is constructed using experimental refractive index data [24]. The thickness of the plate is set as  $t_1 = 10$  nm as a beginning value, and the impact of its position ( $d_1$ ) inside the grating is studied at both cold (insulator) and hot (metal) states, as shown in Fig. 4.2(b) and (c), respectively. The hot state is when the sample is heated up to  $90^\circ\text{C}$  and cold state is the room temperature. From the panel given in Fig 4.2(b), the overall design acts as a narrowband dual absorber in the cold state and the position of  $\text{VO}_2$  layer does not change the spectral responses. This is expected by considering the fact that  $\text{VO}_2$  has a refractive index close to Si with a small extinction coefficient in the insulator phase. Contrarily, in the hot state, the absorption response drastically changes by moving the position of  $\text{VO}_2$  inside the grating where it leads to a broader absorption response as well. All these changes can be more understood by looking at the contour plot given in Fig 4.2(c). At small  $d_1$  values, where the  $\text{VO}_2$  layer is in close vicinity of the bottom mirror (design I), the absorption response resembles that of the insulator

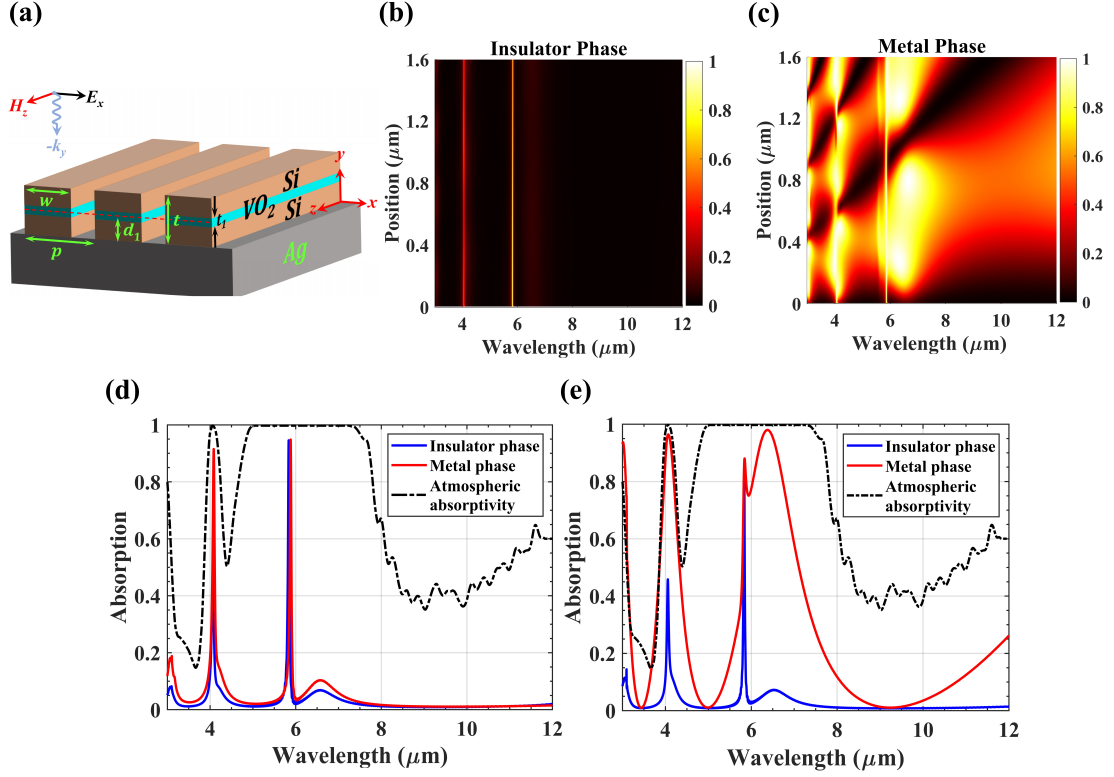


Figure 4.2: (a) Schematic representation of the PCM–dielectric based metamaterial nanoantenna emitter. The contour plots of the absorption amplitude as a function of  $VO_2$  position for (b) insulator and (c) metal phase conditions. The absorption spectra of the structure in both the metallic and insulator phases for two different  $VO_2$  positions at (d)  $d_1 = 5 \text{ nm}$  (design I) and (e)  $d_1 = 1550 \text{ nm}$  (design II).

phase. However, as we move away from the mirror (design II), the bandwidth of the absorption peaks increases. To have a better visualization, the linear plots of the absorption spectra for two different cases of  $d_1 = 5 \text{ nm}$  (design I), and  $d_1 = 1550 \text{ nm}$  (design II) are plotted in Fig. 4.2(d) and (e), respectively. For the  $d_1 = 5 \text{ nm}$  case, the spectra for both insulator and metal phases are similar with a slight red shift at the resonance wavelengths. However, in the  $d_1 = 1550 \text{ nm}$  case, the absorption peaks at the metal phase have been broadened toward the adjacent wavelength ranges. Therefore, spectral responses can be tailored significantly by the position of the  $VO_2$  interlayer and the transition between the phases. The spectral responses of both designs completely match the atmospheric absorption windows.

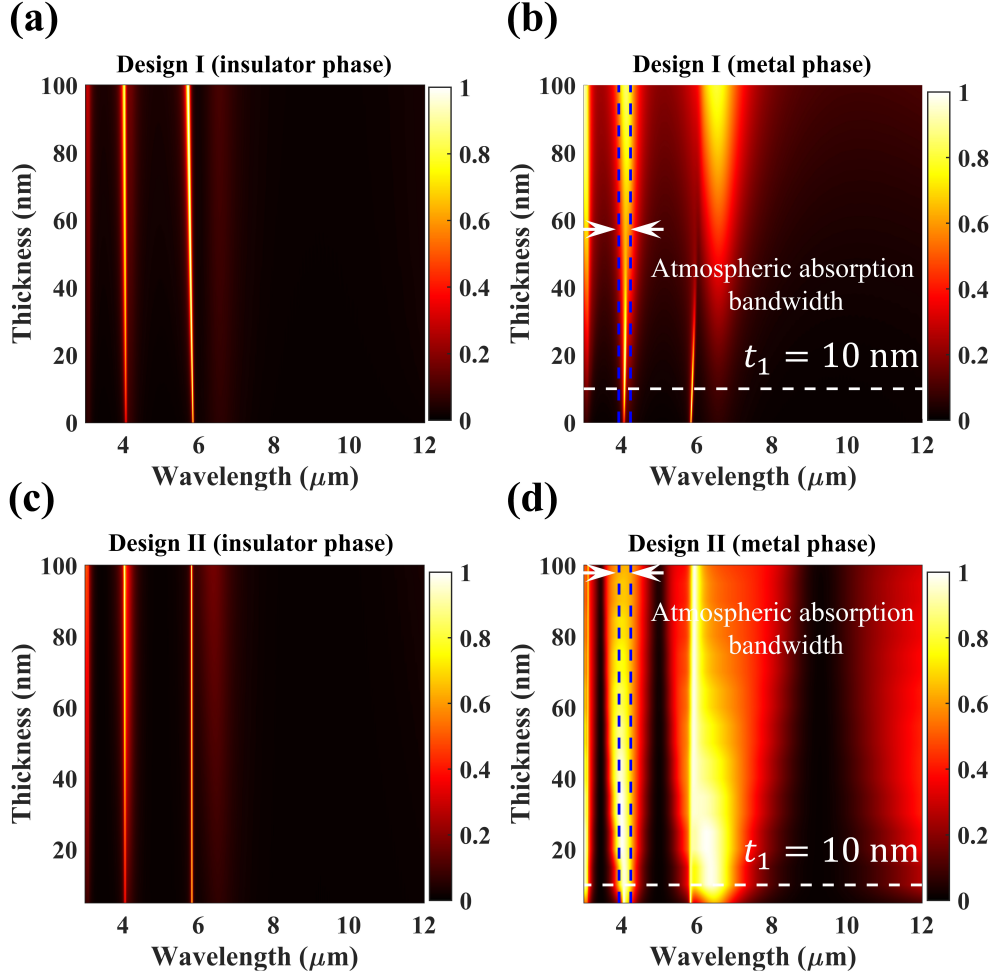


Figure 4.3: Impact of the  $\text{VO}_2$  thickness on the absorption spectrum of design I at (a) the insulator phase, (b) the metallic phase, and on the absorption spectrum of design II at (c) the insulator phase, (d) the metallic phase.

In addition, the thickness of the  $\text{VO}_2$  interlayer is studied as presented in Fig 4.3(a)-(d). According to Figs. 4.3(a) and (c), as the thickness of  $\text{VO}_2$  interlayer increases in the insulator phase, and the amount of absorption of design I and design II slightly increase where the second and third resonances are excited efficiently. However, the changes in the insulator phase are not significant enough to affect the thickness decision.

The main factor in the choice of the thickness is the behavior of the resonances in the metal phase for both design I and design II, as shown in Figs. 4.3(b) and (d). Fig. 4.3(b) demonstrates that increasing the thickness of  $\text{VO}_2$  interlayer

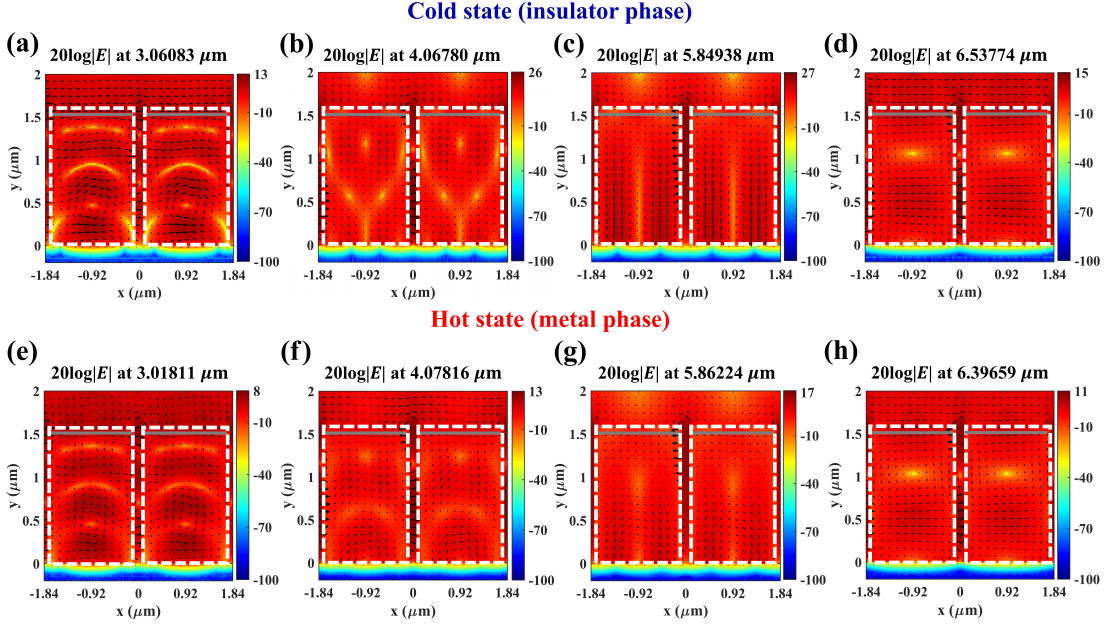


Figure 4.4: On resonance electric-field distributions across the proposed PCM–dielectric based metamaterial nanoantenna emitter (design II) on the  $x$  -  $y$  plane for (a)–(d) the cold and (e)–(h) hot states when the position of  $\text{VO}_2$  interlayer is  $d_1 = 1550$  nm. The color bar is shown in logarithmic scales for better comparison. The thin  $\text{VO}_2$  interlayer is shown as the gray lines within the structure while the Si boundaries are shown as white dashed lines.

causes two important changes in the absorption response of design I in the metallic phase. First, the amount of absorption at the third resonance wavelength, as the most important resonance occurred in the main atmospheric absorption window, starts decreasing. Second, in addition to increasing in the amount of absorption at the first and second resonance wavelengths, these resonances are going to be wider which causes the exceeding of the absorption bandwidth of the corresponding atmospheric windows. Therefore, using a thicker  $\text{VO}_2$  interlayer more than 10 nm is undesirable for design I.

**Table 4.1**

Resonance	1	2	3	4
Insulator phase	3.06083 $\mu\text{m}$	4.06780 $\mu\text{m}$	5.84938 $\mu\text{m}$	6.53774 $\mu\text{m}$
Metal phase	3.01811 $\mu\text{m}$	4.07816 $\mu\text{m}$	5.86224 $\mu\text{m}$	6.39659 $\mu\text{m}$
Relative shift	– 0.0139	0.0025	0.0021	– 0.02159

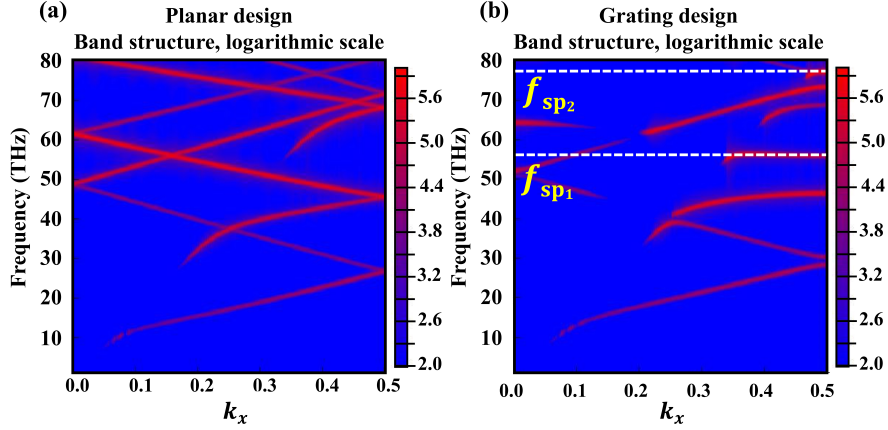


Figure 4.5: Dispersion diagram of the (a) Ag-Si planar structure and the (b) Ag-Si nanograting structure with the dimensions given in Fig. 4.1(a).

Moreover, as seen in Fig. 4.3(d), increasing the thickness of the  $\text{VO}_2$  interlayer reduces the amount of absorption and broadens the width of the resonance wavelengths of design II in the metallic phase. The broader response of the second resonance (as a result of thicker  $\text{VO}_2$  interlayer) can lead to exceeding the absorption bandwidth of the corresponding atmospheric absorption, which is undesirable. Therefore, similar to the design I, selecting the thickness of  $\text{VO}_2$  interlayer around 10 nm can be reasonable and desirable based on the absorption responses of the structure.

To figure out the physical mechanism behind the aforementioned drastic changes, field distribution analyses, and absorbed power density calculations are performed at both metallic and insulator phases of the broadband design (design II). The associated electric-field results on the x - y plane including two periods of the structure are depicted in Figs. 4.4(a)–(h). For better visualization, all of the field distributions are shown in the logarithmic scale. The resonance wavelengths of the broadband design for both metallic and insulator cases are also shown in table 4.1.

As shown in these panels, the electric-field distributions are drastically changed, upon a phase change. In the insulator phase, the on-resonance field profiles (Figs. 4.4(b) and (c)) at Ag-Si interface show the excitation of surface plasmons (SPs). Therefore, the grating design triggers the excitation of SPs and

this leads to narrowband light absorptions in the resonance wavelengths (see Fig. 4.2(e)). However, in the metallic phase (Figs. 4.4(f) and (g)), the formation of standing waves can be seen within the grating design. It can be anticipated that the absorption mechanism is dominantly originated from the formation of Fabry-Perot (FP) like cavity resonances. Therefore, in the insulator phase, plasmonic mode is the dominant mechanism while in metallic phase cavity mode is the main absorption mechanism. In fact, moving from lossless insulator phase to lossy metal one, a virtual metal–insulator–metal (MIM) cavity is created in the grating design. This virtual cavity design supports absorption of the light in a broad spectral range. That is the reason behind the broadening of the absorption response. When the VO<sub>2</sub> interlayer is positioned close to the Ag mirror (design I), this MIM cavity cannot be formed, and the resonance profile does not change between two states.

To further investigate mentioned resonances, dispersion relation of the surface waves supported by unpatterned Ag-Si planar structure is calculated by using a band structure technique of the FDTD method. In this band structure technique, a parameter sweep over the transverse wavevector is carried out, and frequencies with strong resonances are searched. Simulated dispersion relation of this multi-layer system is shown in Fig. 4.5(a). Afterward, the same analysis is performed for the Ag-Si nanograting design, as seen in Fig. 4.5(b). Under normal irradiation, SPs cannot be excited in a planar metal–dielectric design, while diffraction by subwavelength nanograting can excite the plasmonic modes. Thus, the differences on dispersion relations of these two structures provide information about the plasmonic modes excited in the nanograting design. As shown by dotted lines in Fig. 4.5(b), different from planar structure, two SP frequencies of  $f_{sp1}$  and  $f_{sp2}$  are present in the nanograting design. The  $f_{sp1}$  and  $f_{sp2}$  are located at 55 THz ( $\lambda = 5.45 \mu\text{m}$ ) and 76 THz ( $\lambda = 3.95 \mu\text{m}$ ), which are in good agreement with the resonance wavelengths of the Ag-Si nanograting design, presented in Fig. 4.1(b).

The above-mentioned statements can be further confirmed by looking at the power absorption profiles across the cavity design on the x - y plane at different resonance wavelengths. The absorbed power density calculations given in Fig. 4.6 demonstrate that most of the power is lost inside the Ag substrate at the

insulator phase (see Figs. 4.6(a) and (b)), while the most partial amount of the absorption at the metallic phase is due to the loss inside the VO<sub>2</sub> interlayer (see Figs. 4.6(g) and (h)). This confirms the proposed mechanisms where the dominant absorption in the insulator phase was related to SP excitation on the Ag–Si interface, while it was FP (formation of a virtual MIM lossy cavity) in the metallic phase.

Based on the obtained results, the proposed design (design II) can elegantly modulate its response from a narrowband absorber to a broadband one, upon increasing the temperature. In the meantime, the positions of the absorption resonance wavelengths are adopted in a way to occur within atmospheric absorption windows. This makes the coated object stay invisible to the IR thermal cameras and radiatively cool itself according to Kirchhoff’s law. Therefore, the proposed design is an adaptive radiative cooling nanoantenna compatible with thermal camouflage technology.

To verify this capability, emitted power density from the structure is calculated using thermal emission modeling [69]. The model is demonstrated in Fig. 4.7(a). First, due to utilizing a thick layer of Ag as a substrate, the transmission can be ignored, and the surface emissivity can be taken as an absorptivity. Therefore, the surface emissivity can be written as;

$$\varepsilon_{eff}(T, \lambda) = \varepsilon_{structure}(T, \lambda) = 1 - R_{structure}(T, \lambda), \quad (4.1)$$

where  $\varepsilon_{structure}(T, \lambda)$  and  $R_{structure}(T, \lambda)$  are considered as the absorptivity and reflectivity of the proposed nanoantenna emitter dependent on the operating wavelength ( $\lambda$ ) and absolute temperature ( $T$ ) of the body. Then, the blackbody radiation can be calculated by the formula given by [136];

$$BB(T, \lambda) = \frac{2\pi hc^2}{\lambda^5(e^{\frac{hc}{\lambda kT}} - 1)}, \quad (4.2)$$

where  $h$ ,  $c$ , and  $k_B$  are Planck constant, the speed of light in vacuum, and Boltzmann constant. The thermal emission can be obtained as a multiplication of Eq. (4.1) by Eq. (4.2) as;

$$TE(T, \lambda) = \varepsilon_{eff}(T, \lambda)BB(T, \lambda), \quad (4.3)$$

Taking an integral with respect to the wavelengths over the region of interest will give the detected optical power density by the camera as presented in (4.4);

$$P = \int_{\lambda_1}^{\lambda_2} TE(T, \lambda) d\lambda, \quad (4.4)$$

In this work, the wavelength intervals are chosen as 3 - 4  $\mu\text{m}$ , 4 - 4.2  $\mu\text{m}$ , 4.2 - 5  $\mu\text{m}$ , 5 - 8  $\mu\text{m}$  and 8 - 12  $\mu\text{m}$  according to the atmospheric windows over the 3 - 12  $\mu\text{m}$ . The calculated detected power densities for the proposed narrowband structure (design I) are presented in Figs. 4.7(b)–(f) in the logarithmic scale. Due to the hysteresis behavior of  $\text{VO}_2$  around the transition temperature 68 °C, the heating behavior from insulator to metal and cooling behavior from metal to insulator takes different paths in the transition. To make sure the design has thermal camouflage in both cases, the calculations are done separately for cooling and heating conditions. The intervals 4 - 4.2  $\mu\text{m}$  and 5 - 8  $\mu\text{m}$  are the regions of interest that the power emission should be high enough for releasing the energy. In those regions, the released power is expected to be as close as possible to the blackbody radiation so the build-up energy can be released without causing any risk of detection by the IR thermal cameras (see Figs. 4.7(c) and (e)). On the contrary, the rest of the intervals are the ones that the atmospheric windows allow the emission of power. Therefore, any power released in those regions should be as small as possible and far away enough from the blackbody radiation for both cooling and heating conditions that can be observed in Figs. 4.7(b), (d), and (f).

As discussed before, if the placement of the  $\text{VO}_2$  interlayer is arranged to the top part of the Si (design II), the absorption response of the structure at the cold

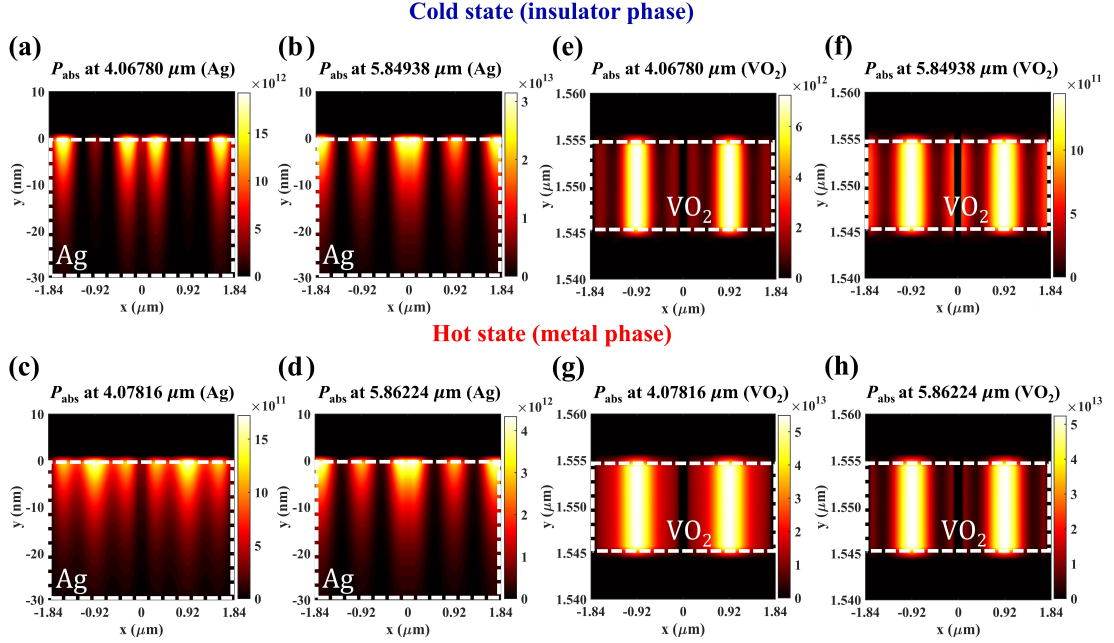


Figure 4.6: On resonance absorbed power density distributions across the Ag layer on the  $x$  -  $y$  plane considering two periodicities for (a), (b) the cold and (c), (d) hot states when the position of  $\text{VO}_2$  interlayer is  $d_1 = 1550$  nm. On resonance absorbed power density distributions across the  $\text{VO}_2$  layer on the  $x$  -  $y$  plane considering two periodicities for (e), (f) the cold and (g), (h) hot states when the position of  $\text{VO}_2$  interlayer is  $d_1 = 1550$  nm.

state (insulator phase) will remain almost the same with design I (both designs have similar absorption responses in the insulator phase, see the blue lines in Figs. 4.2(d) and (e)). However, the hot state (metallic phase) of design II results in response change from the narrowband to the broadband one. The broadband response means a larger thermal power release. Although the resonance peaks become broader in the hot state, they still stay in the atmospheric absorption windows to prevent any detection probability by the IR thermal cameras. The calculations of the detected powers by an IR camera in a logarithmic scale for the proposed broadband structure (design II) are presented in Figs. 4.8(a)–(e). Figs. 4.8(a), (c), and (e) are the calculated powers in the non-absorptive intervals where the powers should place as far as possible from the blackbody radiation. On the other hand, Figs. 4.8(b) and (d) are the regions where the response of the design should be close to the blackbody radiation.

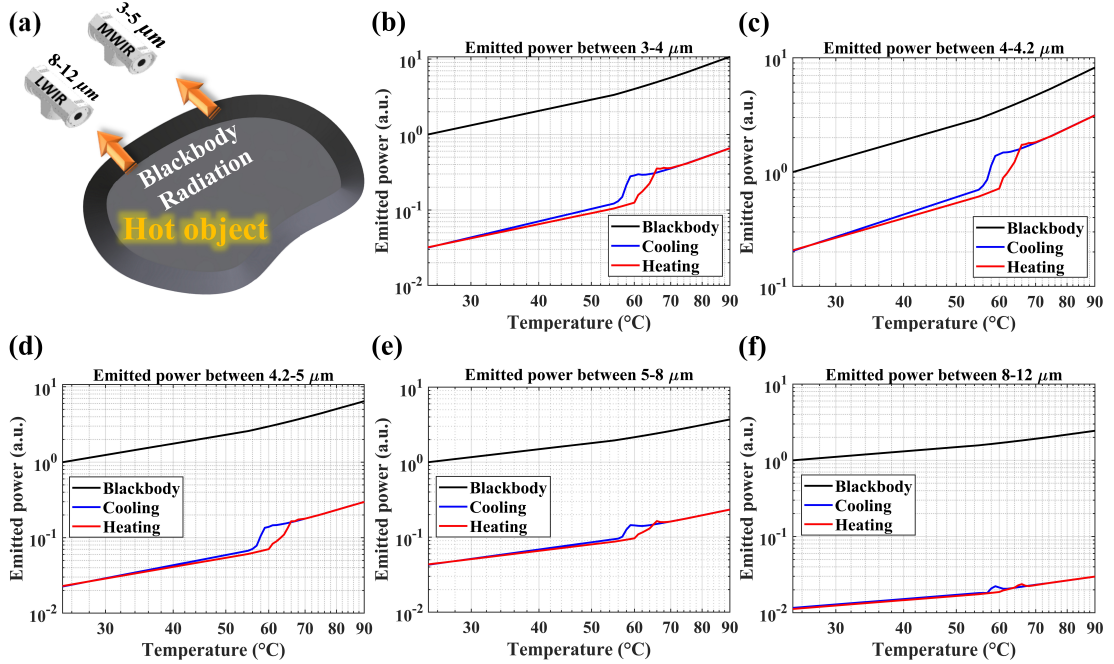


Figure 4.7: . (a) Schematic illustration of the detected optical power density using IR thermal cameras emitted from the proposed PCM–dielectric based metamaterial nanoantenna emitter. Emitted power density calculations of design I given in a logarithmic scale for different intervals including (b) 3 - 4  $\mu\text{m}$ , (c) 4 - 4.2  $\mu\text{m}$ , (d) 4.2 - 5  $\mu\text{m}$ , (e) 5 - 8  $\mu\text{m}$ , and (f) 8 - 12  $\mu\text{m}$ .

The absorption responses and, therefore, the emission responses of the proposed structure, which are placed over the blackbody radiation, for both narrowband and broadband designs (design I and II) in the cold and hot states of the VO<sub>2</sub> interlayer are demonstrated in Fig. 4.9. For a better comparison, blackbody radiations at 25 °C and 90 °C, the emission responses of the proposed designs over the blackbody radiations at four different cases, and real emissions of the proposed designs with consideration of atmospheric transmission spectrum are presented. Both narrowband and broadband responses are quite similar in the cold state (see Figs. 4.9(a) and (c)). Even though sharp emission peaks are displayed around 6  $\mu\text{m}$ , the absorption feature of the atmosphere at that wavelength cancels the aforementioned peak in the real emission and, therefore, the design becomes invisible in the MIR region for both designs in the cold state. For the hot state, the emissions over the blackbody demonstrate different peaks for the

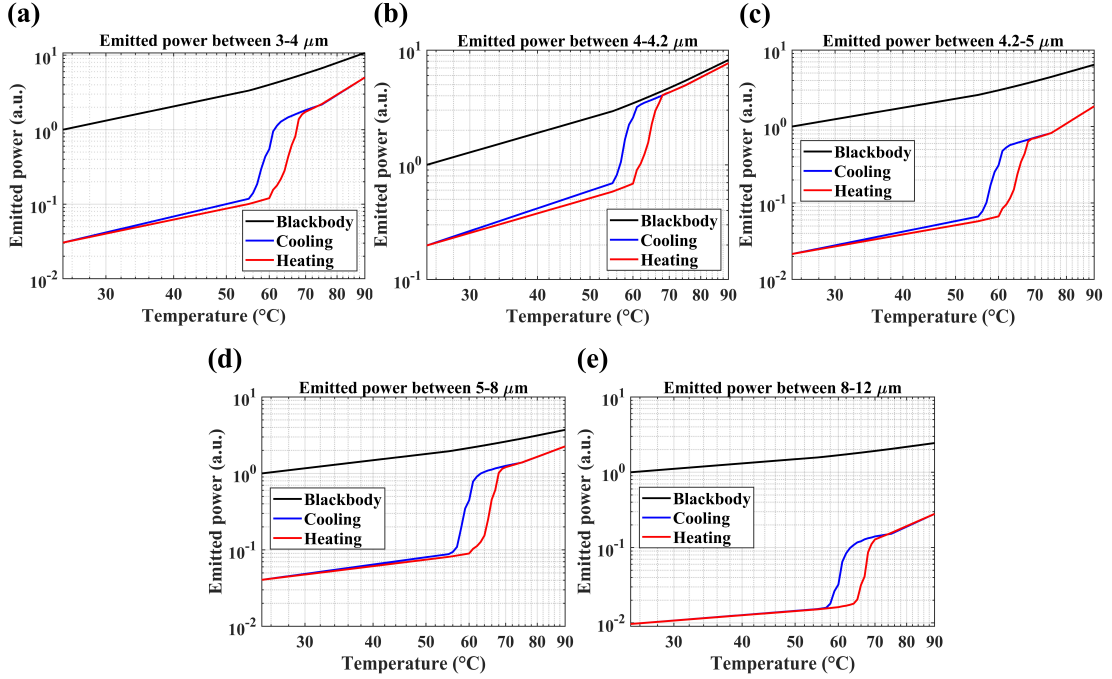


Figure 4.8: Emitted power density calculations of design II given in a logarithmic scale for different intervals including (a) 3 - 4  $\mu\text{m}$ , (b) 4 - 4.2  $\mu\text{m}$ , (c) 4.2 - 5  $\mu\text{m}$ , (d) 5 - 8  $\mu\text{m}$ , and (e) 8 - 12  $\mu\text{m}$ .

narrowband and broadband designs (see Figs. 4.9(b) and (d)). However, consideration of the atmospheric absorption windows cancels most of the emission and invisibility of the design is preserved. It is observed that narrowband design acts better in comparison to broadband design for thermal camouflage applications but being a perfect and broadband absorber within the absorption windows helps more to reduce the coated targets' temperature. This leads to thermal balance and radiative heat exchange between the target and low temperature surrounding.

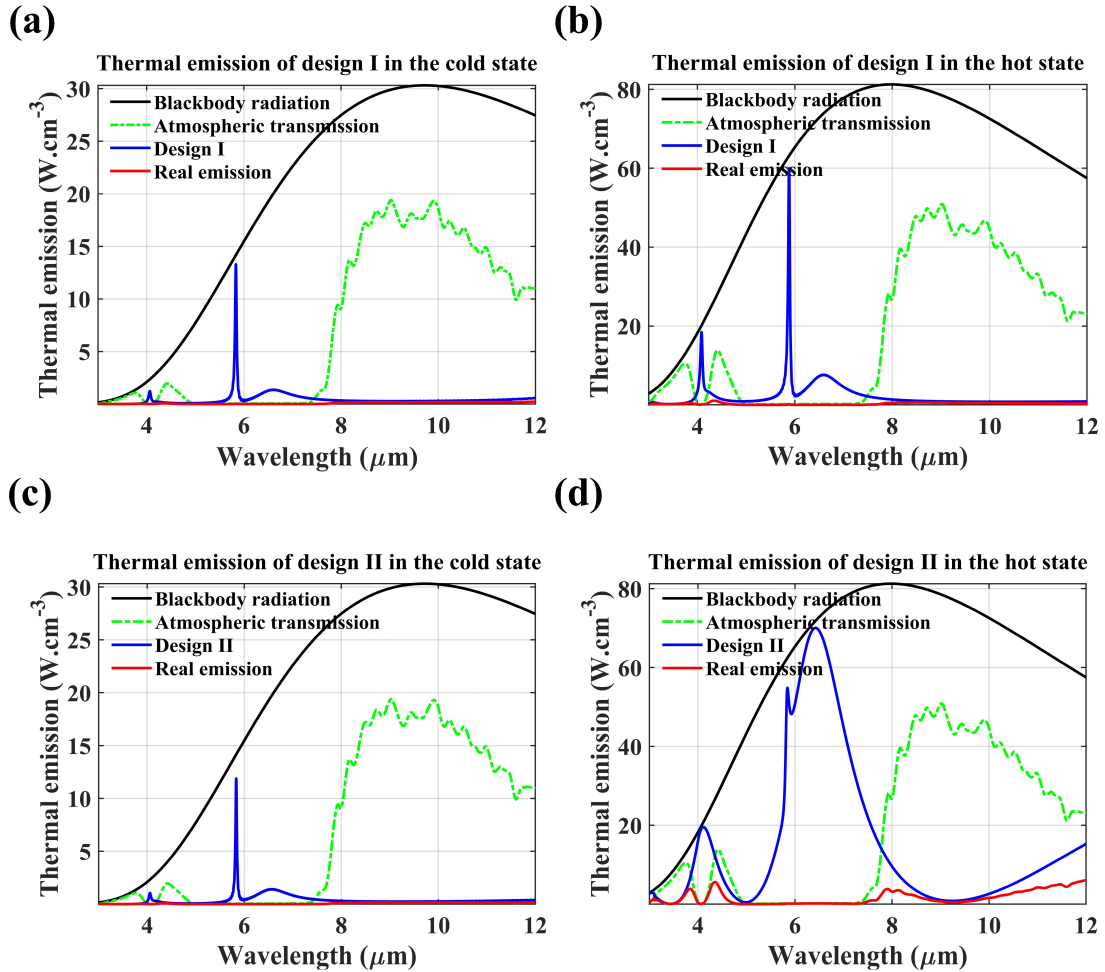


Figure 4.9: Comparisons among the emitted power densities at different temperatures including blackbody radiation (black solid line), atmospheric transmissivity for 5 km long transmission path through the atmosphere at the ground level (green dashed-dotted line) over the corresponding blackbody radiation, the proposed structure without considering atmospheric transmissivity (blue solid line) over the corresponding blackbody radiation, and the real emission response of the proposed design I and II (red solid line). The emitted power densities of the proposed narrowband design at the (a) cold state when the temperature is 25 °C and (b) hot state when the temperature is 90 °C. The emitted power densities of the proposed broadband design at the (c) cold state when the temperature is 25 °C and (d) hot state when the temperature is 90 °C.

# Chapter 5

## An all-dielectric metasurface coupled with two-dimensional semiconductors for thermally tunable ultra-narrowband light absorption

This chapter is one part reprinted with permission from: **Ebru Buhara**, Amir Ghobadi, Ekmel Ozbay, An All-Dielectric Metasurface Coupled with Two-Dimensional Semiconductors for Thermally Tunable Ultra-narrowband Light Absorption, 2020, Plasmonics, 16, 687–694. DOI: 10.1007/s11468-020-01330-4

### 5.1 Introduction

In this section, we propose a dielectric based metasurface platform to achieve ultra-narrowband light absorption within a monolayer thick TMDC layer. For

this purpose, we first optimize the metasurface design itself. Then, we couple this design with mono and multilayer TMDCs to observe better absorption results. For this purpose, we choose MoS<sub>2</sub>, and WS<sub>2</sub> as the most commonly used TMDCs. The coupling of light into Mie resonances, supported by dielectric nanograting, provides narrowband absorption within the TMDC layer. To reach further enhancement, a cavity design is integrated into this dielectric-based metasurface. For the best optimized design, the absorptance efficiency reaches to 0.85 and FWHM stays as narrow as 3.1 nm. Finally, we move one step forward to show the thermal tunability characteristic of our design, without use of any phase change material. This is achieved due to strong light confinement within the design. Due to this confinement, any small change in the refractive index is seen by the resonant design. Thus, the resonance frequency shifts and thermal tunability is acquired. The thermal sensitivity of the above mentioned optimized design reaches to 0.0096 nm/°C.

## 5.2 Results and Discussion

Fig. 5.1(a) is a schematic illustration of the dielectric metasurface design, consisting of nanogratings from titanium dioxide (TiO<sub>2</sub>). Thickness and width of the TiO<sub>2</sub>, and the periodicity of the structure are indicated as  $t$ ,  $w$ , and  $P$ , respectively. The refractive index of TiO<sub>2</sub> is set at 2.3705 at room temperature [137]. The calculations to find optimal geometries and dimensions are performed by a commercial finite-difference time-domain (FDTD) software package (Lumerical FDTD Solutions) [129]. While the numerical calculations are executed, the incident light propagation direction is selected as perpendicular to the x-y plane and, boundary conditions for x and y directions are chosen as periodic boundary and perfectly matched layer (PML) for the z direction.

In standard circumstances, TiO<sub>2</sub> cannot absorb or confine light due to its transparent and lossless nature in the visible range. Using the proposed design in Fig. 5.1(a), Mie resonances can be excited, and it can provide a spectral selective strong confinement of the light. This strong confinement at the resonance

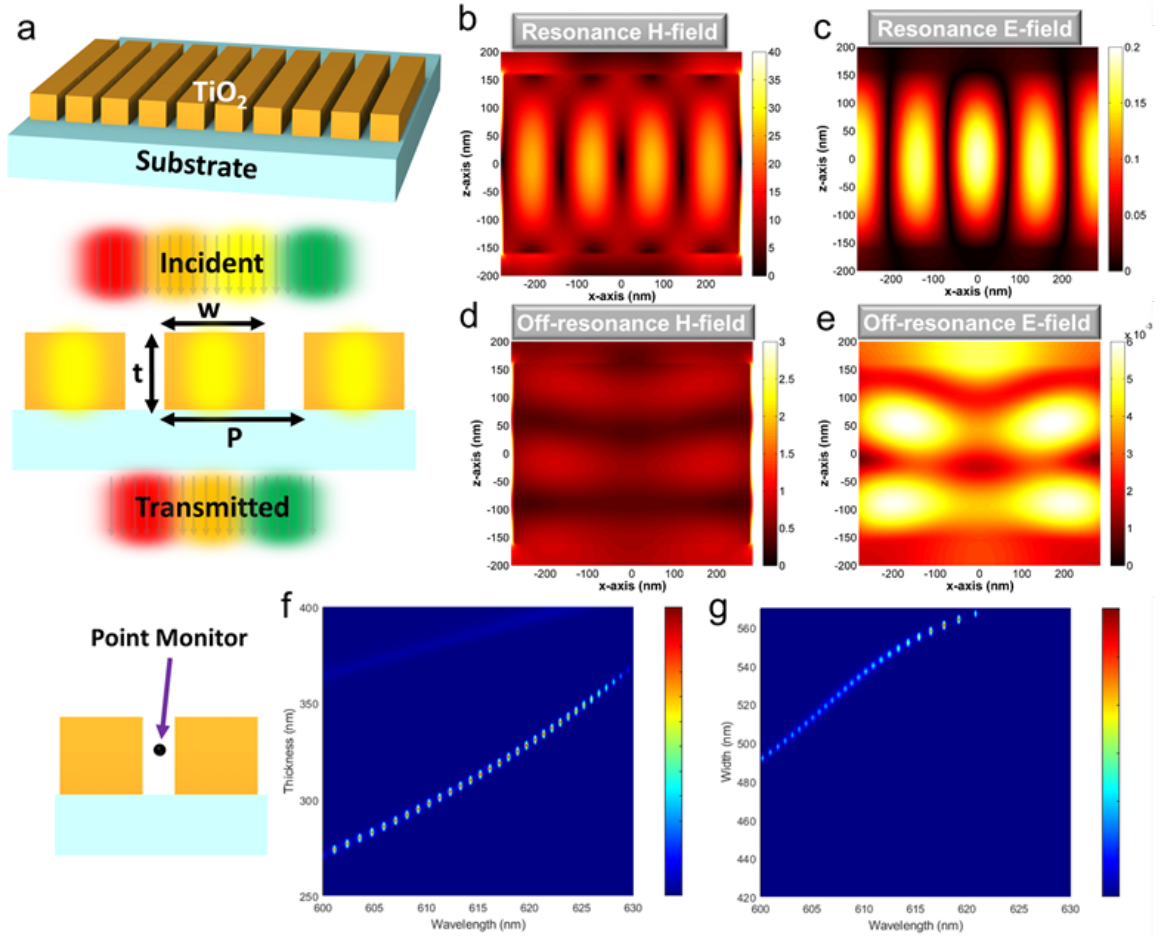


Figure 5.1: (a) Schematic representation of the proposed dielectric metasurface structure. H-field and E-field distributions across the design for (b, c) resonance frequency and (d, e) off-resonance region. Contour plots of magnetic field intensity dependence to (f) thickness and (g) width

frequency can be seen in the E-field and H-field profiles across the structure in the Fig. 5.1(b) and (c). The structure becomes an ordinary transparent dielectric in the of-resonance frequencies, as shown in the Fig. 5.1(d) and (e). The structure has an ability to provide field enhancement, at specific thickness and width values. For better qualitative comparison, the magnetic field intensities are probed at the point monitor position for the desired spectral range. These field intensities are studied for different  $t$  and  $W$  values, while  $P$  is kept as 570 nm in all simulations. The sweeping results are shown as a contour plot in the Fig. 5.1(f) and (g). The contour plots imply that at specific geometrical values the structure provides large absorption cross section. Thus, if a material with

high absorption coefficient is embedded into the bottom of the  $\text{TiO}_2$  grating, spectrally selective light absorption can be achieved, and the structure becomes an ultra-narrow semiconductor absorber.

Monolayer TMDCs are excellent candidates for this purpose. Due to their single atomic-scale thickness, the off-resonance absorption is quite low and this causes a high contrast light absorption.  $\text{MoS}_2$  and  $\text{WS}_2$  as a monolayer from TMDCs are selected for the absorbent semiconductor layer. In their own case, these monolayer materials can only absorb small amount of the incoming power due to its ultrathin thickness of  $\sim 0.62$  nm. To be able to increase the absorptance magnitude, monolayers are coupled to this resonant metasurface design. This metasurface confines a specific wavelength and passes the rest of spectrum. In other words, it can be seen as an ultra-narrowband band-stop filter.

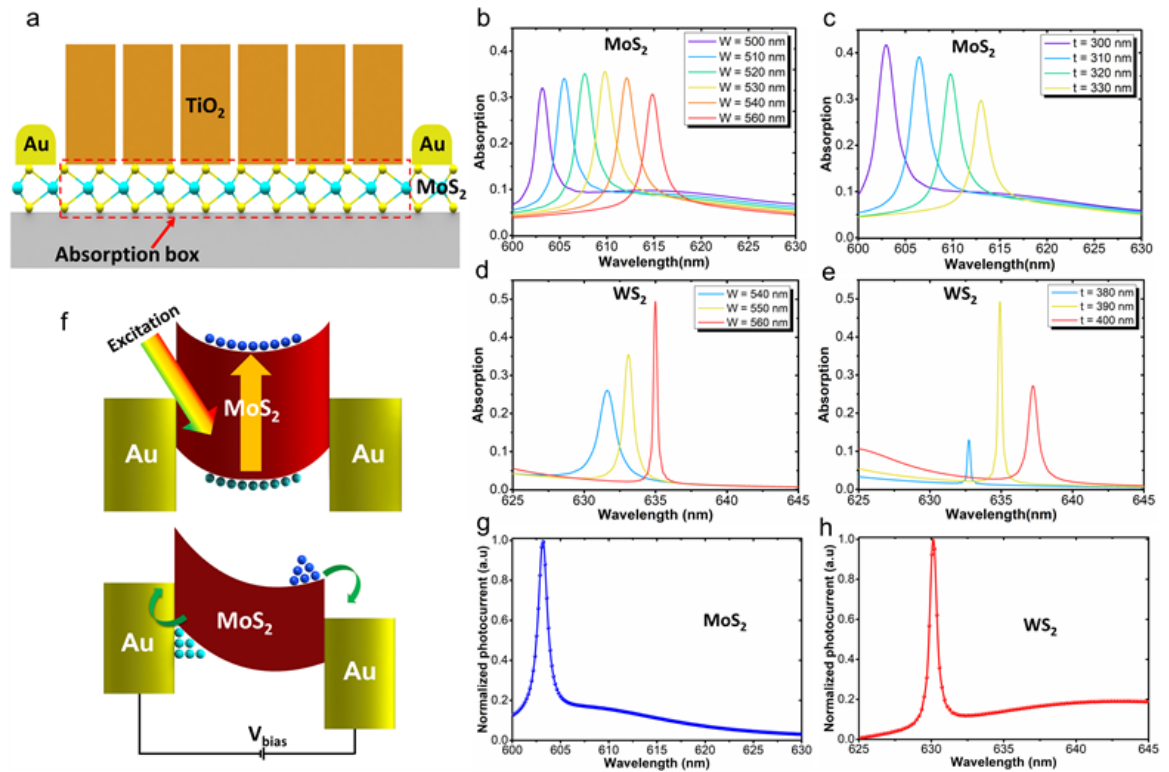


Figure 5.2: (a) Schematic representation of the all-dielectric narrow-band absorber structure, absorption calculation for varying thickness and width of  $\text{TiO}_2$  with  $\text{MoS}_2$  (b–c) and  $\text{WS}_2$  (d–e). (f) The band alignment between Au and  $\text{MoS}_2$  layer before and after applying bias. The simulated photocurrent values generated by TMD monolayers in (g)  $\text{MoS}_2$  and (h)  $\text{WS}_2$  cases.

To examine the absorption features of the structure, MoS<sub>2</sub> is placed right underneath the TiO<sub>2</sub> nano-grating as a monolayer and absorption calculation is taken on the monolayer region. The proposed configuration is shown in the Fig. 5.2(a). Starting with the optimal thickness and width values of the metasurface from previous section, the dependence of spectral absorption within the TMDCs to geometrical values is analyzed with 10-nm intervals in Fig. 5.2(b) and (c). For this purpose, the absorption within the TMDC layer is calculated using below Eq. (5.1).

$$A(\lambda) = \frac{1}{P_{incident}} \iiint 0.5\omega \text{imag}(\epsilon_{MoS_2}) |E(x, y, z, \lambda)|^2 dx dy dz, \quad (5.1)$$

This formula has been used to ensure that the absorption is fully within the layer and parasitic absorption is ignored. After finding the optimum dimensions for the width value, which is 530 nm, thickness optimization is performed with final result of 300 nm. For these geometries, the absorption resonance is located at 603 nm wavelength with a maximum absorptance 0.42 and FWHM of 2.7 nm. The same procedure is applied to the WS<sub>2</sub> monolayer. The strongest absorption peak is found at the 560 nm width and 390 nm thickness, as shown in the Figs. 5.2(d) and (e). The spectral position, amplitude, and FWHM values of this design are 634.9 nm, 0.493, and 0.3 nm.

Thus, the function of proposed metasurface is the selective coupling of the incident light into the TMDC semiconductor monolayer. To convert this structure into the photodetector, Au contacts can be made on its surface to form metal-semiconductor-metal (MSM) configuration. In this design, upon broadband light illumination, mostly photons corresponding to resonance peak position are absorbed and a photocurrent spectrum similar to absorption profile is achieved. This phenomenon is illustrated in the Fig. 5.2 (f). COMSOL Multiphysics finite element method solver is used, to numerically analyze the photo-electrical response of the photodetector. As shown in Figs. 5.2(g) and (h), the proposed design can provide an order of magnitude larger photocurrents in the resonance peak, compared with of-resonance ones. Thus, the proposed configuration can be

utilized to accomplish an ultra-narrowband 2D photodetector

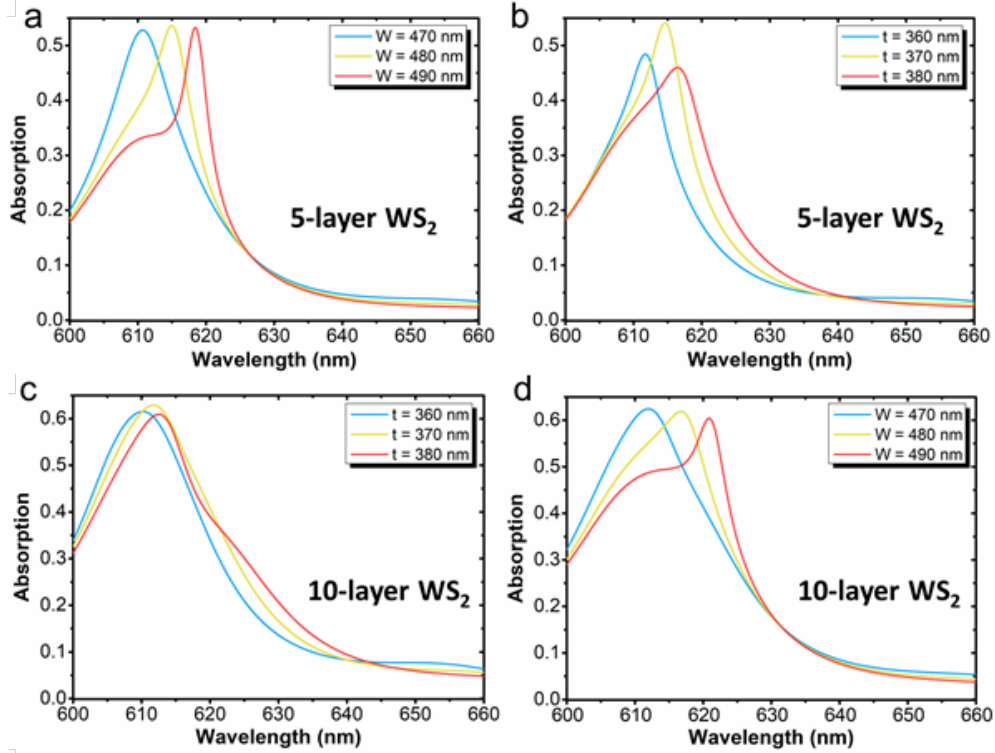


Figure 5.3: Absorption calculation for varying (a) thickness and (b) width of  $\text{TiO}_2$  with 5 Layer  $\text{WS}_2$  and varying (c) thickness and (d) width of  $\text{TiO}_2$  with 10 Layer  $\text{WS}_2$

While the absorption peak for both  $\text{MoS}_2$  and  $\text{WS}_2$  is quite narrow FWHM, the absorbance amplitude is much below unity. To be able to increase the amplitude towards the unity, two approach can be proposed: (i) increasing the semiconductor layer thickness and (ii) using cavity design to improve light trapping. To examine the first idea, 5-layer, and 10-layer  $\text{WS}_2$  are placed instead of the monolayer. The similar optimization process is conducted to get the highest absorption peak. The results are presented in Figs. 5.3(a-d). The maximum value is increased up to 0.55 with 5-layer and 0.63 with 10-layer configurations. However, this improvement is achieved in the expense of broadening of FWHM (15.1 nm for 5-layer, and 23.1 nm for 10-layer), and increasing the background absorption, compared with that of monolayer (see Figs. 5.2(d) and (e)). This higher of-resonance absorption is the result of thicker semiconductor layer. Thus, in this configuration, although the amplitude has been gradually improved, the

selectivity (the ratio of resonance and off-resonance absorptions) is decreased and FWHM is widened. For the second approach, the proposed metasurface design is placed on top of a metal-insulator (MI) cavity. Fig. 5.4(a) is an illustration of the cavity enhanced design. Silver (Ag) is chosen as the bottom metal mirror. As shown in the absorption per unit volume plot, the dominant part of the absorption occurs within the TMDC monolayer and minor part is lost as parasitic absorption (Jule loss) within the bulk metal. The width and thickness value of TiO<sub>2</sub> is optimized in Fig. 5.4(c) and Fig. 5.4(d) for MoS<sub>2</sub> and Fig. 5.4(e) and Fig. 5.4(f) for WS<sub>2</sub>. The optimal absorption values are much higher compared to previous designs. For MoS<sub>2</sub> case, cavity design has improved absorptance to a value as high as 0.85 with a FWHM of 3.1 nm. While, WS<sub>2</sub> cavity design absorptance value is reached to 0.72 at with a FWHM as narrow as 1.4 nm.

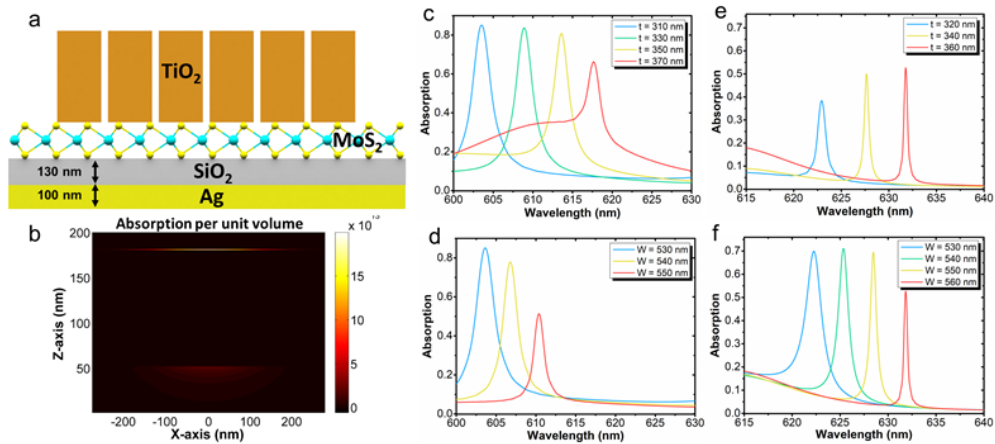


Figure 5.4: (a) Proposed optimized cavity design and (b) its absorption profile across the cavity with MoS<sub>2</sub> and absorption calculation for varying thickness and width of TiO<sub>2</sub> with MoS<sub>2</sub> (c-d) and (e-f) WS<sub>2</sub>

Besides having high magnetic field enhancement, the structure is also sensitive to the environment temperature. As schematically illustrated in Fig. 5.5 (a), the structure has thermally tunable absorption response. This is due to strong field confinement within the nanogratings. Changing temperature cause the change in the refractive index of the TiO<sub>2</sub> material. Although TiO<sub>2</sub> has very small thermo-optic coefficient of  $\sim 4.2 \times 10^{-5}$ , the formation of hot spots in small volume fractions triggers the high sensitivity of the resonance mode into environmental index change. Thus, the change in temperature is resulted with the shift in the

absorption spectrum. To show this effect refractive index of  $\text{TiO}_2$  is swept from 2.36 to 2.5 with 0.01 intervals. This effect is shown with both  $\text{MoS}_2$  and  $\text{WS}_2$  material in the Figs. 5.5 (a) and (b). These results are indicated that the design can act as an ultra-narrowband single-color detector, without using any phase change material. The thermal sensitivity graphics of the cavity design for each monolayer are also shown in the Figs. 5.5 (d) and (e). The sensitivity values for  $\text{MoS}_2$  and  $\text{WS}_2$ -based designs are  $0.0096 \text{ nm}/^\circ\text{C}$  and  $0.0099 \text{ nm}/^\circ\text{C}$ , respectively. These values are significantly high compared with inherent small thermo-optic coefficient of  $\text{TiO}_2$ .

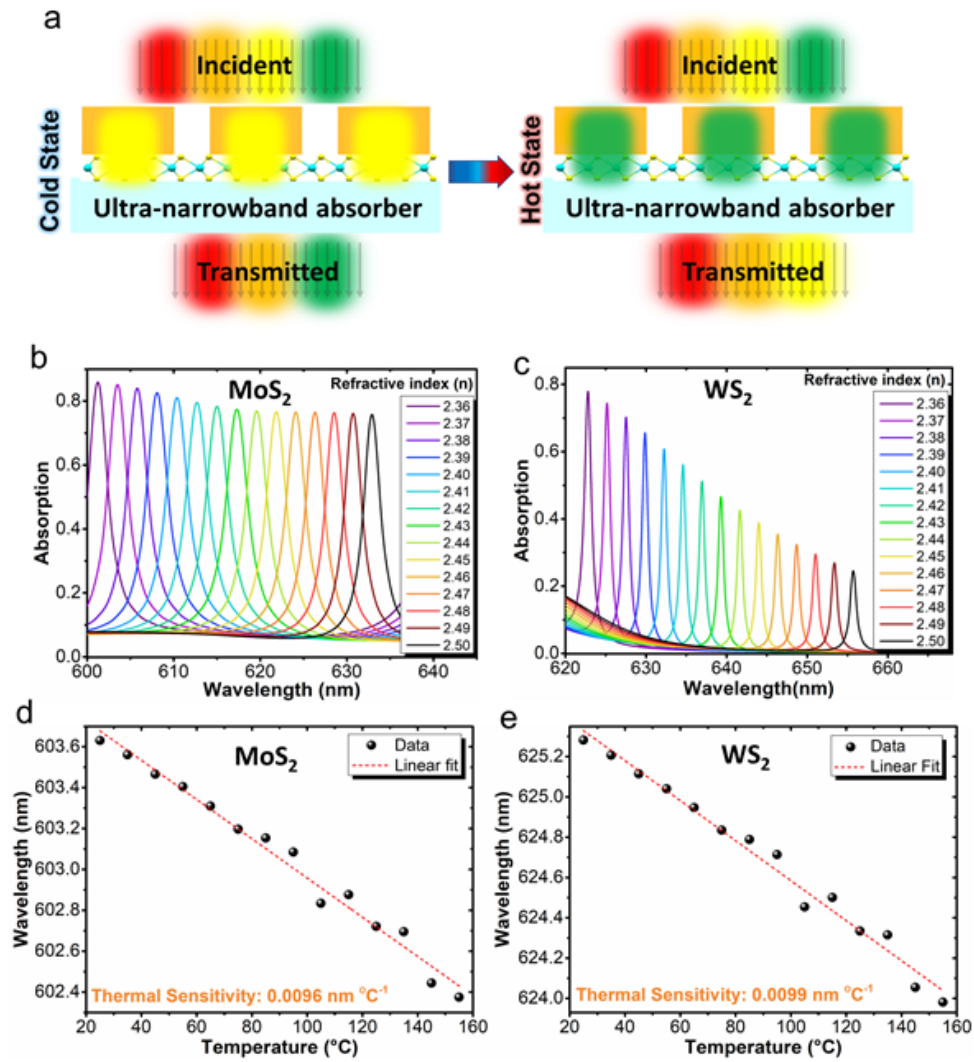


Figure 5.5: (a) Schematic illustration of red-shift of the absorption peak as the temperature is increased. Absorption calculation for varying refractive index of TiO<sub>2</sub> with (b) MoS<sub>2</sub> and (c) WS<sub>2</sub> in the proposed design and thermal sensitivity plots with different temperature for (d) MoS<sub>2</sub> and (e) WS<sub>2</sub>

# Chapter 6

## Conclusion

This thesis demonstrated and discussed important functionalities of adaptive metasurfaces, namely, dynamically tunable metasurface for adaptive visible and short-wave infrared camouflage, nanoantenna emitter for multi-spectral infrared camouflage, phase-change material coupled dielectric nanoantenna for mid-infrared adaptive thermal camouflage, and an all-dielectric metasurface for thermally tunable ultra-narrowband light absorption.

In chapter 2, an adaptive metasurface design is demonstrated with tunable optical responses in both visible and SWIR ranges. The proposed design acts as a transmissive color filter in the amorphous phase and, upon a temperature increase, it turns into a reflective mirror. In the meantime, this phase transition provides the opportunity for the real-time tuning of the SWIR mode response of the design to cover a broad range and adaptive camouflage.

In chapter 3, the study demonstrates a visible-transparent infrared selective emitter capable of multi-spectral camouflage in SWIR, MWIR, and LWIR modes. The proposed design can also radiatively cool itself in the NTIR windows.

In chapter 4, the study demonstrates a thermally tunable nanoantenna emitter based on a hybrid design made of a metamaterial absorber and VO<sub>2</sub> thin film as a PCM for thermal camouflage applications. The camouflage capability of the

proposed design is in-depth studied using numerical analyses. It was found that an ultrathin VO<sub>2</sub> embedded layer can significantly tailor the antenna response. In the cold state, the absorption response is not VO<sub>2</sub> position dependent and the dominant harvesting mechanism is due to the excitation of plasmonic mode formed in the metal–dielectric interface. On the other hand, the response in the hot state can be effectively manipulated from narrowband (design I) to broadband (design II) by changing the position of the VO<sub>2</sub> thin film. However, in both cases, we adopt a design that is precisely matched the atmospheric absorption windows. Thus, this tunable nanoantenna emitter releases its heat energy into the atmosphere through the absorption windows in the spectrum. The power emission suppression is achieved only at the atmospheric windows and the verification of this behavior is demonstrated with the emitted power calculations over the selected intervals for both narrowband (design I) and broadband (design II) responses. Due to the hysteresis behavior of the VO<sub>2</sub>, the calculations are carried out separately under cooling and heating conditions. Calculated power densities demonstrate the superiority of the proposed designs for being utilized in the thermal camouflage applications.

In chapter 5, the study is focused to enhance the absorption of TMDCs specifically MoS<sub>2</sub> and WS<sub>2</sub> monolayer with the help of the all-dielectric metasurface structure. The absorption behavior of the proposed structure is an ultranarrowband response over the visible range. The cavity design and multilayer approaches are studied for the further enhancement of the absorptance amplitude. The cavity approach was shown to be a promising approach to maximize the performance of the design. Due to strong field confinement, the proposed design revealed thermally tunable absorption response, without the use of phase-change component. This paper proposes a universal design approach that can be used in other 2D and ultrathin optical systems where strong and selective light absorption can be achieved in atomic scale dimensions. The tunability added to this design provides the opportunity to realize multi-color photodetectors using the same design. As temperature changes, the absorption peak experiences a spectral shift and by this way we can detect different colors using the same photodetector design. Besides, this design has the ability to be used in sensing

application as well. As an unknown agent is coated on the grating surface, the resonance peak will shift, and from the produced shift value, one can estimate the refractive index of the material.

# Bibliography

- [1] G. Singh, Rajni, and A. Marwaha, “A review of metamaterials and its applications,” *International Journal of Engineering Trends and Technology (IJETT)*, 2015.
- [2] J. Hu, S. Bandyopadhyay, Y. Liu, and L. Shao, “A review on metasurface: From principle to smart metadevices,” *Frontiers in Physics*, 2021.
- [3] A. J. Hoffman, L. Alekseyev, S. S. Howard, K. J. Franz, D. Wasserman, V. A. Podolskiy, E. E. Narimanov, D. L. Sivco, and C. Gmachl, “Negative refraction in semiconductor metamaterials,” 2007.
- [4] D. R. Smith, J. B. Pendry, and M. C. Wiltshire, “Metamaterials and negative refractive index,” 2004.
- [5] G. T. Papadakis, D. Fleischman, A. Davoyan, P. Yeh, and H. A. Atwater, “Optical magnetism in planar metamaterial heterostructures,” *Nature Communications*, 2018.
- [6] C. Menzel, C. Helgert, C. Rockstuhl, E. B. Kley, A. Tünnermann, T. Pertsch, and F. Lederer, “Asymmetric transmission of linearly polarized light at optical metamaterials,” *Physical Review Letters*, 2010.
- [7] J. Valentine, J. Li, T. Zentgraf, G. Bartal, and X. Zhang, “An optical cloak made of dielectrics,” *Nature Materials*, 2009.
- [8] D. Schurig, J. J. Mock, B. J. Justice, S. A. Cummer, J. B. Pendry, A. F. Starr, and D. R. Smith, “Metamaterial electromagnetic cloak at microwave frequencies,” *Science*, 2006.

- [9] A. Fang, T. Koschny, and C. M. Soukoulis, “Lasing in metamaterial nanostructures,” *Journal of Optics A: Pure and Applied Optics*, 2010.
- [10] E. Plum, V. A. Fedotov, P. Kuo, D. P. Tsai, and N. I. Zheludev, “Towards the lasing spaser: controlling metamaterial optical response with semiconductor quantum dots,” *Optics Express*, 2009.
- [11] V. G. Veselago, “The electrodynamics of substances with simultaneously negative values of  $\epsilon$  and  $\mu$ ,” *Sov. Phys.Usp.*, 1968.
- [12] J. Pendry, A. Holden, D. Robbins, and W. Stewart, “Low frequency plasmons for thin-wire structure,” *J. Phys. Condens.*, 1998.
- [13] B. Wu, W. Wang, J. Pacheco, X. Chen, T. Grzegorzcyk, and J. A. Kong, “A study of using metamaterial as antenna substrates to enhance gain,” *Progress in Electromagnetic Research*, 2005.
- [14] A. K. Osgouei, H. Hajian, A. E. Serebryannikov, and E. Ozbay, “Hybrid indium tin oxide-au metamaterial as a multiband bi-functional light absorber in the visible and near-infrared ranges,” *Journal of Physics D: Applied Physics*, 2021.
- [15] H. Kocer, H. Isik, Y. Durna, B. Khalichi, H. Kurt, and E. Ozbay, “Nano shell impact on huygens’ metasurface dipolar resonances and optical response,” *JOSA B*, 2021.
- [16] T. Ellenbogen, K. Seo, and K. B. Crozier, “Chromatic plasmonic polarizers,”
- [17] C. Ji, K. T. Lee, T. Xu, J. Zhou, H. J. Park, and L. J. Guo, “Engineering light at the nanoscale: Structural color filters and broadband perfect absorbers,” *Advanced Optical Materials*, 2017.
- [18] N. I. Landy, C. M. Bingham, T. Tyler, N. Jokerst, D. R. Smith, and W. J. Padilla, “Design, theory, and measurement of a polarization-insensitive absorber for terahertz imaging,” *Physical Review B - Condensed Matter and Materials Physics*, 2009.

- [19] P. Offermans, M. C. Schaafsma, S. R. Rodriguez, Y. Zhang, M. Crego-Calama, S. H. Brongersma, and J. G. Rivas, “Universal scaling of the figure of merit of plasmonic sensors,” *ACS Nano*, 2011.
- [20] M. E. Stewart, C. R. Anderton, L. B. Thompson, J. Maria, S. K. Gray, J. A. Rogers, and R. G. Nuzzo, “Nanostructured plasmonic sensors,” *Advanced Optical Materials*, 2008.
- [21] A. Tittl, A. K. U. Michel, M. Schöferling, X. Yin, B. Gholipour, L. Cui, M. Wuttig, T. Taubner, F. Neubrech, and H. Giessen, “A switchable mid-infrared plasmonic perfect absorber with multispectral thermal imaging capability,” *Advanced Materials*, 2015.
- [22] J. K. Tong, W. C. Hsu, Y. Huang, S. V. Boriskina, and G. Chen, “Thin-film ‘thermal well’ emitters and absorbers for high-efficiency thermophotovoltaics,” *Scientific Reports*, 2015.
- [23] W. Li and J. Valentine, “Metamaterial perfect absorber based hot electron photodetection,” *Nano Letters*, 2014.
- [24] Y. Zhai, Y. Ma, S. N. David, D. Zhao, R. Lou, G. Tan, R. Yang, and X. Yin, “Scalable-manufactured randomized glass-polymer hybrid metamaterial for daytime radiative cooling,” *Science*, 2017.
- [25] S. Xiao, T. Wang, T. Liu, C. Zhou, X. Jiang, and J. Zhang, “Active metamaterials and metadevices: a review,” *J. Phys. D: Appl. Phys.*, 2020.
- [26] F. Neubrech, X. Duan, and N. Liu, “Dynamic plasmonic color generation enabled by functional materials,” *Science Advances*, 2020.
- [27] J. He, M. Zhang, S. Shu, Y. Yan, and M. Wang, “ $\text{Vo}_2$  based dynamic tunable absorber and its application in switchable control and real-time color display in the visible region,” *Optics Express*, 2020.
- [28] B. Ko, T. Badloe, and J. Rho, “Vanadium dioxide for dynamically tunable photonics,” *ChemNanoMat*, 2021.

- [29] Q. He, N. Youngblood, Z. Cheng, X. Miao, and H. Bhaskaran, “Dynamically tunable transmissive color filters using ultra-thin phase change materials,” *Optics Express*, 2020.
- [30] M. Jafari, L. J. Guo, and M. Rais-Zadeh, “A reconfigurable color reflector by selective phase change of gete in a multilayer structure,” *Advanced Optical Materials*, 2019.
- [31] H. Liu, W. Dong, H. Wang, L. Lu, Q. Ruan, Y. S. Tan, R. E. Simpson, and J. K. W. Yang, “Rewritable color nanoprints in antimony trisulfide films,” *Science Advances*, 2020.
- [32] M. Delaney, I. Zeimpekis, D. Lawson, D. W. Hewak, and O. L. Muskens, “A new family of ultralow loss reversible phase-change materials for photonic integrated circuits:  $\text{Sb}_2\text{S}_3$  and  $\text{sb}_2\text{se}_3$ ,” *Advanced Functional Materials*, 2020.
- [33] R. Hu, S. Huang, M. Wang, X. Luo, J. Shiomi, and C. W. Qiu, “Encrypted thermal printing with regionalization transformation,” *Advanced Materials*, 2019.
- [34] E. Buhara, A. Ghobadi, B. Khalichi, H. Kocer, and E. Ozbay, “Mid-infrared adaptive thermal camouflage using a phase-change material coupled dielectric nanoantenna,” *J. Phys. D: Appl. Phys.*, 2021.
- [35] L. Xiao, H. Ma, J. Liu, W. Zhao, Y. Jia, Q. Zhao, K. Liu, Y. Wu, Y. Wei, S. Fan, and K. Jiang, “Fast adaptive thermal camouflage based on flexible  $\text{vo}_2$ /graphene/cnt thin films,” *Nano Letters*, 2015.
- [36] A. K. Osgouei, H. Hajian, B. Khalichi, A. E. Serebryannikov, A. Ghobadi, and E. Ozbay, “Active tuning from narrowband to broadband absorbers using a sub-wavelength  $\text{vo}_2$  embedded layer,” *Plasmonics*, 2021.
- [37] J. Song, S. Huang, Y. Ma, Q. Cheng, R. Hu, and X. Luo, “Radiative metasurface for thermal camouflage, illusion and messaging,” *Optics Express*, 2020.

- [38] W. Xi, Y. Liu, J. Song, R. Hu, and X. Luo, “High-throughput screening of a high-q mid-infrared tamm emitter by material informatics,” *Optics Letters*, 2021.
- [39] A. K. Osgouei, A. Ghobadi, B. Khalichi, and E. Ozbay, “A spectrally selective gap surface-plasmon-based nanoantenna emitter compatible with multiple thermal infrared applications,” *Journal of Optics*, 2014.
- [40] H. Zhu, Q. Li, C. Tao, Y. Hong, Z. Xu, W. Shen, S. Kaur, P. Ghosh, and M. Qiu, “Anomalous collapses of nares strait ice arches leads to enhanced export of arctic sea ice,” *Nature Communications*, 2021.
- [41] X. Feng, X. Xie, M. Pu, X. Ma, Y. Guo, X. Li, and X. Luo, “Hierarchical metamaterials for laser-infrared-microwave compatible camouflage,” *Optics Express*, 2020.
- [42] Y. Qu, Q. Li, L. Cai, M. Pan, P. Ghosh, K. Du, and M. Qiu, “Thermal camouflage based on the phase-changing material gst,” *Light: Science Applications*, 2018.
- [43] B. Khalichi, A. Ghobadi, A. K. Osgouei, and E. Ozbay, “Diode like high-contrast asymmetric transmission of linearly polarized waves based on plasmon-tunneling effect coupling to electromagnetic radiation modes,” *J. Phys. D: Appl. Phys.*, 2021.
- [44] G. Dayal and S. A. Ramakrishna, “Broadband infrared metamaterial absorber with visible transparency using ito as ground plane,” *Optics Express*, 2014.
- [45] Y. Wang, A. C. Overvig, S. Shrestha, R. Zhang, R. Wang, N. Yu, and L. D. Negro, “Tunability of indium tin oxide materials for mid-infrared plasmonics applications,” *Optical Materials Express*, 2017.
- [46] B. Zhao and Z. M. Zhang, “Resonance perfect absorption by exciting hyperbolic phonon polaritons in 1d hbn gratings,” *Optics Express*, 2017.

- [47] B. Zhao and Z. M. Zhang, “Perfect mid-infrared absorption by hybrid phonon-plasmon polaritons in hbn/metal-grating anisotropic structures,” *International Journal of Heat and Mass Transfer*, 2017.
- [48] M. Planck, “Ueber das gesetz der energieverteilung im normalspectrum,” *Ann. Phys.*, 1901.
- [49] J. Stefan, “Über die beziehung zwischen der wärmestrahlung und der temperatur, sitzungsberichte der mathematisch-naturwissenschaftlichen classe der kaiserlichen,” *Akad. Wiss*, 1879.
- [50] G. Kirchhoff, “Über das verhältnis zwischen dem emissionsvermögen und dem absorptionsvermögen der körper für wärme und licht,” *Von Kirchhoff Bis Planck: Theorie Der Wärmestrahlung in Historisch-kritischer Darstellung*, 1978.
- [51] D. G. Baranov, Y. Xiao, I. A. Nechepurenko, A. Krasnok, A. Alu, and M. A. Kats, “Nanophotonic engineering of far-field thermal emitters,” *Nat. Mater*, 2019.
- [52] H. Zhu, Q. Li, C. Zheng, Y. Hong, Z. Xu, H. Wang, W. Shen, S. Kaur, P. Ghosh, and M. Qiu, “High-temperature infrared camouflage with efficient thermal management,” *Light Sci. Appl.*, 2020.
- [53] M. Pan, Y. Huang, Q. Li, H. Luo, H. Zhu, A. Kaur, and M. Qiu, “Multi-band middle-infrared-compatible camouflage with thermal management via simple photonic structures,” *Nano Energy*, 2020.
- [54] T. Kim, J.-Y. Bae, N. Lee, and H. H. Cho, “Hierarchical metamaterials for multispectral camouflage of infrared and microwaves,” *Adv. Funct. Mater*, 2019.
- [55] M. Zeyghami, D. Y. Goswami, and E. Stefanakos, “A review of clear sky radiative cooling developments and applications in renewable power systems and passive building cooling,” *Sol. Energy Mater. Sol. Cells*, 2018.
- [56] C. Xu, G. T. Stiubianu, and A. A. Gorodetsky, “Adaptive infrared-reflecting systems inspired by cephalopods,” *Science*, 2018.

- [57] N. Baranwal and S. P. Mahulikar, “Infrared signature of aircraft engine with choked converging nozzle,” *J. Thermophys. Heat Transfer*, 2016.
- [58] X. Xie, X. Li, M. Pu, X. Ma, K. Liu, Y. Guo, and X. Luo, “Plasmonic metasurfaces for simultaneous thermal infrared invisibility and holographic illusion,” *Adv. Funct. Mater.*, 2018.
- [59] L. Phan, W. G. Walkup, D. D. Ordinario, E. Karshalev, J.-M. Jocson, A. M. Burke, and Gorodetsky, “Reconfigurable infrared camouflage coatings from a cephalopod protein,” *Adv. Mater.*, 2013.
- [60] A. Berk, P. Conforti, R. Kennett, T. Perkins, F. Hawes, and B. J. van Den, “Modtran® 6: a major upgrade of the modtran® radiative transfer code,” *6th Workshop on Hyperspectral Image and Signal Processing: Evolution in Remote Sensing (WHISPERS)*, 2014.
- [61] M. A. Kats, R. Blanchard, S. Zhang, P. Genevet, C. Ko, S. Ramanathan, and F. Capasso, “Vanadium dioxide as a natural disordered metamaterial: perfect thermal emission and large broadband negative differential thermal emittance,” *Phys. Rev.*, 2013.
- [62] Y. Qu, Q. Li, K. Du, L. Cai, J. Lu, and M. Qiu, “Dynamic thermal emission control based on ultrathin plasmonic metamaterials including phase-changing material gst,” *Laser Photonics Rev.*, 2017.
- [63] E. Buhara, A. Ghobadi, and E. Ozbay, “An all-dielectric metasurface coupled with two-dimensional semiconductors for thermally tunable ultra-narrowband light absorption,” *Plasmonics*, 2020.
- [64] S. Abdollahramezani, “Dynamic hybrid metasurfaces,” *Nano Letters*, 2021.
- [65] S. Abdollahramezani, O. Hemmatyar, H. Taghinejad, A. Krasnok, Y. Kiarashinejad, M. Zandehshahvar, A. Alu, and A. Adibi, “Tunable nanophotonics enabled by chalcogenide phase-change materials,” *Nanophotonics*, 2020.

- [66] P. Guo, A. M. Sarangan, and I. Agha, “A review of germanium-antimony-telluride phase change materials for non-volatile memories and optical modulators,” *Appl. Sci.*, 2019.
- [67] D. Fan, Q. Li, Y. Xuan, H. Tan, and J. Fang, “Temperature-dependent infrared properties of ca doped (la, sr)mno<sub>3</sub> compositions with potential thermal control application,” *Appl. Therm. Eng.*, 2013.
- [68] A. Shahsaf, “Temperature-independent thermal radiation,” *Proc. Natl Acad. Sci. USA*, 2019.
- [69] H. Kocer, M. C. Cakir, Y. Durna, M. C. Soydan, O. Odabasi, H. Isik, K. Aydin, and E. Ozbay, “Exceptional adaptable mwir thermal emission for ordinary objects covered with thin vo<sub>2</sub> film,” *J. Quant. Spectrosc. Radiat. Transfer*, 2021.
- [70] G. Cesarini, G. Leahu, A. Belardini, M. Centini, R. L. Voti, and C. Sibilìa, “Quantitative evaluation of emission properties and thermal hysteresis in the mid-infrared for a single thin film of vanadium dioxide on a silicon substrate,” *Int. J. Therm. Sci.*, 2019.
- [71] X. Wang, Y. Cao, Y. Zhang, L. Yan, and Y. Li, “Fabrication of vo<sub>2</sub>-based multilayer structure with variable emittance,” *Appl. Surf. Sci.*, 2015.
- [72] M. Holynska, A. Tighe, and C. Semprimoschnig, “Coatings and thin films for spacecraft thermo-optical and related functional applications,” *Adv. Mater. Interfaces*, 2018.
- [73] C. O. F. Ba, S. T. Bah, M. D’Auteuil, V. Fortin, P. V. Ashrit, and R. Vallée, “Vo<sub>2</sub> thin films based active and passive thermochromic devices for energy management applications,” *Curr. Appl Phys*, 2014.
- [74] F. J. Morin, “Oxides which show a metal-to-insulator transition at the neel temperature,” *Phys. Rev. Lett.*, 1959.
- [75] D. Liu, H. Ji, R. Peng, H. Cheng, and C. Zhang, “Infrared chameleon-like behavior from vo<sub>2</sub> (m) thin films prepared by transformation of metastable

- vo<sub>2</sub> (b) for adaptive camouflage in both thermal atmospheric windows,” *Sol. Energy Mater. Sol. Cells*, 2018.
- [76] Y. Ke, S. Wang, G. Liu, M. Li, T. J. White, and Y. Long, “Vanadium dioxide: the multistimuli responsive material and its applications,” *Small*, 2018.
- [77] M. Gurvitch, S. Luryi, A. Polyakov, and A. Shabalov, “Nonhysteretic behavior inside the hysteresis loop of vo<sub>2</sub> and its possible application in infrared imaging,” *J. Appl. Phys.*, 2009.
- [78] O. A. Novodvorsky, L. S. Parshina, A. A. Lotin, V. A. Mikhalevsky, O. D. Khramova, E. A. Cherebylo, and P. V. Ya, “Vanadium- and titanium dioxide-based memristors fabricated via pulsed laser deposition,” *J. Surf. Invest.*, 2018.
- [79] S. Cueff, D. Li, Y. Zhou, F. J. Wong, J. A. Kurvits, S. Ramanathan, and R. Zia, “Dynamic control of light emission faster than the lifetime limit using vo<sub>2</sub> phase-change,” *Nat. Commun.*, 2015.
- [80] K.-S. Kim, E.-W. Son, J. W. Youn, and D. U. Kim, “Intense pulsed light sintering of vanadium dioxide nanoparticle films and their optical properties for thermochromic smart window,” *Mater. Des.*, 2019.
- [81] M. C. Cakir, H. Kocer, Y. Durna, D. U. Yildirim, A. Ghobadi, H. Hajian, K. Aydin, H. Kurt, N. Saglam, and E. Ozbay, “Unveiling the optical parameters of vanadium dioxide in the phase transition region: a hybrid modeling approach,” *RSC Adv.*, 2020.
- [82] D. U. Yildirim, A. Ghobadi, M. C. Soydan, O. Atesal, A. Toprak, M. D. Caliskan, and E. Ozbay, “Disordered and densely packed ito nanorods as an excellent lithography-free optical solar reflector metasurface,” *ACS Photonics*, 2019.
- [83] Q. H. Wang, K. Kalantar-Zadeh, and A. Kis, “Electronics and optoelectronics of two-dimensional transition metal dichalcogenides,” *Nat Nanotechnol*, 2012.

- [84] K. S. Novoselov, D. Jiang, F. Schedin, T. J. Booth, V. V. Khotkevich, S. V. Morozov, and A. K. Geim, “Two-dimensional atomic crystals,” *Proc Natl Acad Sci USA*, 2005.
- [85] A. H. C. Neto and K. Novoselov, “Two-dimensional crystals: beyond graphene,” *Mater Express*, 2011.
- [86] C. Dean, A. Young, and I. Meric, “Boron nitride substrates for high-quality graphene electronics,” *Nature Nanotech*, 2010.
- [87] K. S. Novoselov, A. K. Geim, S. V. Morozov, D. Jiang, Y. Zhang, S. V. Dubonos, I. V. Grigorieva, and A. A. Firsov, “Electric field effect in atomically thin carbon films,” *Sci*, 2004.
- [88] F. Schwierz, “Graphene transistors,” *Nature Nanotech*, 2010.
- [89] A. Grigorenko, M. Polini, and K. Novoselov, “Graphene plasmonics,” *Nature Photon*, 2012.
- [90] F. Xia, T. Mueller, and Y. Lin, “Ultrafast graphene photodetector,” *Nature Nanotech*, 2009.
- [91] K. Novoselov, V. Falco, and L. Colombo, “A roadmap for graphene,” *Nature*, 2012.
- [92] B. Peng, P. K. Ang, and K. P. Loh, “Two-dimensional dichalcogenides for light-harvesting applications,” *Nano Today*, 2015.
- [93] H. Li, Y. Shi, M. H. Chiu, and L. J. Li, “Emerging energy applications of two-dimensional layered transition metal dichalcogenides,” *Nano Energy*, 2015.
- [94] Z. Li and S. L. Wong, “Functionalization of 2d transition metal dichalcogenides for biomedical applications,” *Mater Sci Eng*, 2017.
- [95] S. J. McDonnell and R. M. Wallace, “Atomically-thin layered films for device applications based upon 2d tmcd materials,” *Thin Solid Films*, 2016.

- [96] M. I. Pech-Canul and N. M. Ravindra, "Semiconductors: synthesis, properties and applications," *Springer*, 2019.
- [97] A. Geim and I. Grigorieva, "Van der waals heterostructures," *Nature*, 2013.
- [98] H. Li, J. Wu, Z. Yin, and H. Zhang, "Preparation and applications of mechanically exfoliated single-layer and multilayer mos<sub>2</sub> and wse<sub>2</sub> nanosheets," *Acc Chem Res*, 2014.
- [99] K. Kang, S. Xie, and L. Huang, "High-mobility three-atom-thick semiconducting films with wafer-scale homogeneity," *Nature*, 2015.
- [100] M. Chhowalla, H. Shin, and G. Eda, "The chemistry of two-dimensional layered transition metal dichalcogenide nanosheets," *Nature Chem*, 2013.
- [101] F. Xia, H. Wang, and D. Xiao, "Two-dimensional material nanophotonics," *Nature Photon*, 2014.
- [102] S. Wu, S. Buckley, and J. Schaibley, "Monolayer semiconductor nanocavity lasers with ultralow thresholds," *Nature*, 2015.
- [103] Y. Xue, Y. Zhang, Y. Liu, H. Liu, and J. Song, "Scalable production of a few-layer mos<sub>2</sub>/ws<sub>2</sub> vertical heterojunction array and its application for photodetectors," *ACS Nano*, 2016.
- [104] H. S. Lee, S.-W. Min, Y.-G. Chang, M. K. Park, T. Nam, H. Kim, J. H. Kim, S. Ryu, and S. Im, "Mos<sub>2</sub> nanosheet phototransistors with thickness-modulated optical energy gap," *Nano Lett*, 2012.
- [105] D. Akinwande, N. Petrone, and J. Hone, "Two-dimensional flexible nanoelectronics," *Nat Commun*, 2014.
- [106] B. Radisavljevic, A. Radenovic, J. Brivio, V. Giacometti, and A. Kis, "Single-layer mos<sub>2</sub> transistors," *Nat Nanotechnol*, 2011.
- [107] C. Xie and F. Yan, "Flexible photodetectors based on novel functional materials," *Small*, 2017.

- [108] M. Bernardi, M. Palummo, and J. C. Grossman, “Extraordinary sunlight absorption and one nanometer thick photovoltaics using two-dimensional monolayer materials,” *Nano Lett*, 2013.
- [109] A. Ghobadi, T. G. U. Ghobadi, F. Karadas, and E. Ozbay, “Semiconductor thin film based metasurfaces and metamaterials for photovoltaic and photoelectrochemical water splitting applications,” *Adv Opt Mater*, 2019.
- [110] W. Chen, L. Wang, Y. Jiang, and J. Wang, “A perfect absorber based on monolayer  $\text{mos}_2$  and nano-silver in the visible regime,” *2018 International Conference on Microwave and Millimeter Wave Technology (ICMMT)*, 2018.
- [111] D. Huo, J. Zhang, and H. Wang, “Broadband perfect absorber with monolayer  $\text{mos}_2$  and hexagonal titanium nitride nano-disk array,” *Nanoscale Res Lett*, 2017.
- [112] S. M. Bahauddin, H. Robotjazi, and I. Thomann, “Broadband absorption engineering to enhance light absorption in monolayer  $\text{mos}_2$ ,” *ACS Photonics*, 2016.
- [113] K. Zhou, J. Song, L. Lu, Z. Luo, and Q. Cheng, “Plasmon-enhanced broadband absorption of  $\text{mos}_2$ -based structure using au nanoparticles,” *Opt Express*, 2016.
- [114] J. Song, L. Lu, Q. Cheng, and Z. Luo, “Surface plasmon-enhanced optical absorption in monolayer  $\text{mos}_2$  with one-dimensional au grating,” *J Quant Spectrosc Radiat Transf*, 2018.
- [115] S. Butun, E. Palacios, J. D. Cain, Z. Liu, V. P. Dravid, and K. Aydin, “Quantifying plasmon-enhanced light absorption in monolayer  $\text{ws}_2$  films,” *ACS Appl Mater Interfaces*, 2017.
- [116] X. Jiang, T. Wang, S. Xiao, X. Yan, L. Cheng, and Q. Zhong, “Approaching perfect absorption of monolayer molybdenum disulfide at visible wavelengths using critical coupling,” *Nanotechnol*, 2018.

- [117] X. Fang, Q. Tian, and G. Yang, “Enhanced absorption of monolayer molybdenum disulfide ( $\text{mos}_2$ ) using nanostructures with symmetrical cross resonator in the visible ranges,” *Opt. Quant Electron*, 2019.
- [118] J. H. Sr, Y. Ren, Y. Qing, H. Li, E. Yao, X. Wu, W. Liu, and W. Xie, “Dual-band total absorption via guided-mode resonance in a monolayer  $\text{mos}_2$  covered dielectric grating structure,” *Nanophotonics and Micro/Nano Optics IV*, 2018.
- [119] Y. M. Qing, H. F. Ma, S. Yu, and T. J. Cui, “Ultra-narrowband absorption enhancement in monolayer transition-metal dichalcogenides with simple guided-mode resonance filters,” *J Appl Phys*, 2019.
- [120] J. Nong, H. Da, Q. Fang, Y. Yu, and X. Yan, “Perfect absorption in transition metal dichalcogenides-based dielectric grating,” *J Phys D: Appl Phys*, 2018.
- [121] J. T. Liu, T. B. Wang, X. J. Li, and N. H. Liu, “Enhanced absorption of monolayer  $\text{mos}_2$  with resonant back reflector,” *J Appl Phys*, 2014.
- [122] H. Lu, X. Gan, D. Mao, Y. Fan, D. Yang, and J. Zhao, “Nearly perfect absorption of light in monolayer molybdenum disulfide supported by multilayer structures,” *Opt Express*, 2017.
- [123] A. Ghobadi, H. Hajian, B. Butun, and E. Ozbay, “Strong light-matter interaction in lithography-free planar metamaterial perfect absorbers,” *ACS Photonics*, 2018.
- [124] D. U. Yildirim, A. Ghobadi, M. C. Soydan, A. E. Serebryannikov, and E. Ozbay, “One-way and near-absolute polarization insensitive near-perfect absorption by using an all-dielectric metasurface,” *Opt Lett*, 2020.
- [125] D. U. Yildirim, A. Ghobadi, and E. Ozbay, “Near-absolute polarization insensitivity in graphene based ultra-narrowband perfect visible light absorber,” *Sci Rep*, 2018.

- [126] D. U. Yildirim, “Colorimetric and near-absolute polarization-insensitive refractive-index sensing in all-dielectric guided-mode resonance based meta-surface,” *J Phys Chem C*, 2019.
- [127] M. C. Soydan, A. Ghobadi, D. U. Yildirim, V. B. Erturk, and E. Ozbay, “All ceramic-based metal-free ultra-broadband perfect absorber,” *Plasmonics*, 2019.
- [128] P. B. Johnson and R. W. Christy, “Optical constants of the noble metals,” *Phys. Rev. B*, 1972.
- [129] L. S. Inc.
- [130] I. Abdulhalim, “Coupling configurations between extended surface electromagnetic waves and localized surface plasmons for ultrahigh field enhancement,” *Nanophotonics*, 2018.
- [131] J. Kischkat, S. Peters, B. Gruska, M. Semtsiv, M. Chashnikova, M. Klinkmüller, O. Fedosenko, S. Machulik, A. Aleksandrova, G. Monastyrskyi, Y. Flores, and W. T. Masselink, “Mid-infrared optical properties of thin films of aluminum oxide, titanium dioxide, silicon dioxide, aluminum nitride, and silicon nitride,” *Applied Optics*, 2012.
- [132] M. Abutoama and I. Abdulhalim, “Angular and intensity modes self-referenced refractive index sensor based on thin dielectric grating combined with thin metal film,” *IEEE J. Sel. Top. Quantum Electron*, 2017.
- [133] D. V. Nesterenko, S. Hayashi, and Z. Sekkat, “Evanescent-field-coupled guided-mode sensor based on a waveguide grating,” *Appl. Opt*, 2015.
- [134] S. Randhawa, M. U. González, J. Renger, S. Enoch, and R. Quidant, “Design and properties of dielectric surface plasmon bragg mirrors,” *Opt. Express*, 2010.
- [135] D. R. Lide, “Crc handbook of chemistry and physics,” *Boca Raton, FL: CRC Press*, 2004.
- [136] M. Planck, “The theory of heat radiation,” *New York: Courier Corporation*, 2013.

- [137] M. R. Saleem, S. Honkanen, and J. Turunen, “Thermal properties of  $\text{tio}_2$  films fabricated by atomic layer deposition,” *IOP Conf Ser Mater Sci Eng*, 2019.

# Appendix A

## Scientific Contributions

### A.1 Journal Articles

[1] E. Buhara, A. Ghobadi, E. Ozbay. 2021. "Multi-spectral infrared camouflage through excitation of plasmon-phonon polaritons in a visible-transparent hBN-ITO nanoantenna emitter." *Optics Letters*, Vol. 46, Issue 19, pp. 4996-4999.

[2] E. Buhara, A. Ghobadi, E. Ozbay. 2021. "Adaptive visible and short-wave infrared camouflage using a dynamically tunable metasurface." *Optics Letters*, Vol. 46, Issue 19, pp. 4777-4780.

[3] E. Buhara, A. Ghobadi, B. Khalichi, H. Kocer, E. Ozbay. 2021. "Mid-infrared adaptive thermal camouflage using a phase-change material coupled dielectric nanoantenna." *Journal of Physics D: Applied Physics*, 54 265105.

[4] E. Buhara, A. Ghobadi, E. Ozbay. 2020. "An All-Dielectric Metasurface Coupled with Two-Dimensional Semiconductors for Thermally Tunable Ultra-narrowband Light Absorption." *Plasmonics*, 16, 687–694.

## A.2 Conference Papers

[1] A. K. Osgouei, B. Khalichi, E. Buhara, A. Ghobadi, and E. Ozbay, 2021, “Dualband polarization insensitive metamaterial-based absorber suitable for sensing applications,”.

[2] A. K. Osgouei, E. Buhara, B. Khalichi, A. Ghobadi, and E. Ozbay, 2021, “Wavelength selectivity in a polarization-insensitive metamaterial-based absorber consistent with atmospheric absorption windows,”.

[3] B. Khalichi, A. K. Osgouei, E. Buhara, H. Kocer, A. Ghobadi, and E. Ozbay, 2021, “Active thermally tunable samarium nickelate-based nanoantenna emitter,”.

[4] B. Khalichi, E. Buhara, A. K. Osgouei, A. Ghobadi, and E. Ozbay, 2021, “High contrast asymmetric transmission based on the outcoupling of surface plasmon polaritons to radiation modes,”.

[5] E. Buhara, A. K. Osgouei, B. Khalichi, H. Kocer, A. Ghobadi, and E. Ozbay, 2021, “Thermally tunable from narrowband to broadband metamaterialbased nanoantenna emitter,”.